ARTICLE

https://doi.org/10.1038/s41586-018-0469-4

Malaria parasite translocon structure and mechanism of effector export

Chi-Min Ho[1,2,3], Josh R. Beck[4,5,6], Mason Lai[2], Yanxiang Cui[7], Daniel E. Goldberg[4,5], Pascal F. Egea[1,3]* & Z. Hong Zhou[1,2,7]*

The putative *Plasmodium* translocon of exported proteins (PTEX) is essential for transport of malarial effector proteins across a parasite-encasing vacuolar membrane into host erythrocytes, but the mechanism of this process remains unknown. Here we show that PTEX is a bona fide translocon by determining structures of the PTEX core complex at near-atomic resolution using cryo-electron microscopy. We isolated the endogenous PTEX core complex containing EXP2, PTEX150 and HSP101 from *Plasmodium falciparum* in the 'engaged' and 'resetting' states of endogenous cargo translocation using epitope tags inserted using the CRISPR–Cas9 system. In the structures, EXP2 and PTEX150 interdigitate to form a static, funnel-shaped pseudo-seven-fold-symmetric protein-conducting channel spanning the vacuolar membrane. The spiral-shaped AAA+ HSP101 hexamer is tethered above this funnel, and undergoes pronounced compaction that allows three of six tyrosine-bearing pore loops lining the HSP101 channel to dissociate from the cargo, resetting the translocon for the next threading cycle. Our work reveals the mechanism of *P. falciparum* effector export, and will inform structure-based design of drugs targeting this unique translocon.

Malaria has devastated major civilizations since the dawn of humanity, and remains a considerable burden to society; it is responsible for more than 200 million cases and nearly half a million deaths each year[1]. This infectious disease is caused by *Plasmodium* parasites, which invade and reproduce within human erythrocytes, inducing the clinical symptoms of malaria[2,3]. These parasites export hundreds of effector proteins that extensively remodel host erythrocytes, which have limited capacity for biosynthesis[4–6]. Collectively known as the exportome, these proteins create the infrastructure necessary to import nutrients, export waste, and evade splenic clearance of infected erythrocytes[7]. Most of these proteins bear a five-residue motif called the *Plasmodium* export element (PEXEL)[8–10]. The malaria parasite conceals itself inside a parasitophorous vacuole, which is derived from invagination of the host cell plasma membrane during invasion[11] (Fig. 1a). Following secretion into the parasitophorous vacuole, proteins destined for export are unfolded and transported across the parasitophorous vacuole membrane (PVM) into the host cell in an ATP-dependent process[12,13]. To accomplish this, it has been hypothesized that the parasite has evolved a unique membrane protein complex, the *Plasmodium* translocon of exported proteins (PTEX)[14]. PTEX is the only known point of entry to the host cell for exported proteins and is therefore an attractive drug target, as disrupting PTEX blocks delivery of key virulence determinants and induces parasite death[15,16].

PTEX has been proposed to be a membrane protein complex larger than 1.2 MDa, with a core composed of the HSP101 ATPase and two novel proteins, PTEX150 and EXP2[14,17] (Fig. 1a). HSP101 belongs to the class 1 Clp/HSP100 family of AAA+ ATPases, PTEX150 has no known homologues beyond the *Plasmodium* genus, and EXP2 is a PVM protein[14,18] that is conserved among vacuole-dwelling apicomplexans[19]. All three core components are essential for protein export and parasite survival[15,16,20]. A model of PTEX-mediated translocation has been proposed, in which HSP101 unfolds and threads proteins through an oligomeric EXP2 transmembrane channel spanning the PVM, with PTEX150 having a structural role between EXP2 and HSP101[14–17]. However, without structural information, the global architecture of PTEX, the stoichiometry of its components and its molecular mechanism have remained unclear.

In this study, we purify PTEX directly from the human malaria parasite *P. falciparum* and determine the structure of the complex in multiple functional states at near-atomic resolution using cryo-electron microscopy (cryo-EM). Our atomic models reveal the architecture and mechanism of this unique translocon and open a path towards development of novel therapeutics against this promising anti-malarial drug target.

Architecture of the PTEX core complex

To purify PTEX from *P. falciparum*, we used CRISPR–Cas9 editing to introduce a 3×Flag epitope tag on the C terminus of endogenously expressed HSP101 (Extended Data Fig. 1a–c) and purified the endogenously assembled PTEX core complex directly from *P. falciparum* cultured in human erythrocytes (Extended Data Fig. 1d–f). Cryo-EM analysis yielded two distinct conformations of PTEX particles, one extended (195 Å) and the other compact (175 Å) (Fig. 1b, c, Extended Data Table 1). Endogenous cargo polypeptide densities are visible in the central pore of HSP101 in both structures (Fig. 1b, c, Extended Data Figs. 2, 3). On the basis of differences in the arrangement of HSP101 subunits relative to the cargo between the two conformations, we designated them as the 'engaged' and 'resetting' states, respectively. Both maps are at near-atomic resolution, varying from 3.0–3.6 Å in the transmembrane and core regions to 5–8 Å in the periphery (Fig. 1b, c, Extended Data Fig. 4). As most regions exhibit clear sidechain densities throughout both maps (Fig. 1b, c, Extended Data Fig. 5, Supplementary Videos 1, 2) we were able to build de novo atomic models of the three constituent proteins for both conformational states (Fig. 1d, e). Each model contains 20 subunits with 6,898 modelled amino acid residues. Models of all subunits were built independently, as their conformations varied.

[1]The Molecular Biology Institute, University of California, Los Angeles, CA, USA. [2]Department of Microbiology, Immunology & Molecular Genetics, University of California, Los Angeles, CA, USA. [3]Department of Biological Chemistry, David Geffen School of Medicine, University of California, Los Angeles, CA, USA. [4]Department of Medicine, Division of Infectious Diseases, Washington University School of Medicine, St. Louis, MO, USA. [5]Department of Molecular Microbiology, Washington University School of Medicine, St. Louis, MO, USA. [6]Department of Biomedical Sciences, Iowa State University, Ames, IA, USA. [7]California NanoSystems Institute, University of California, Los Angeles, CA, USA. *e-mail: pegea@mednet.ucla.edu; hong.zhou@UCLA.edu

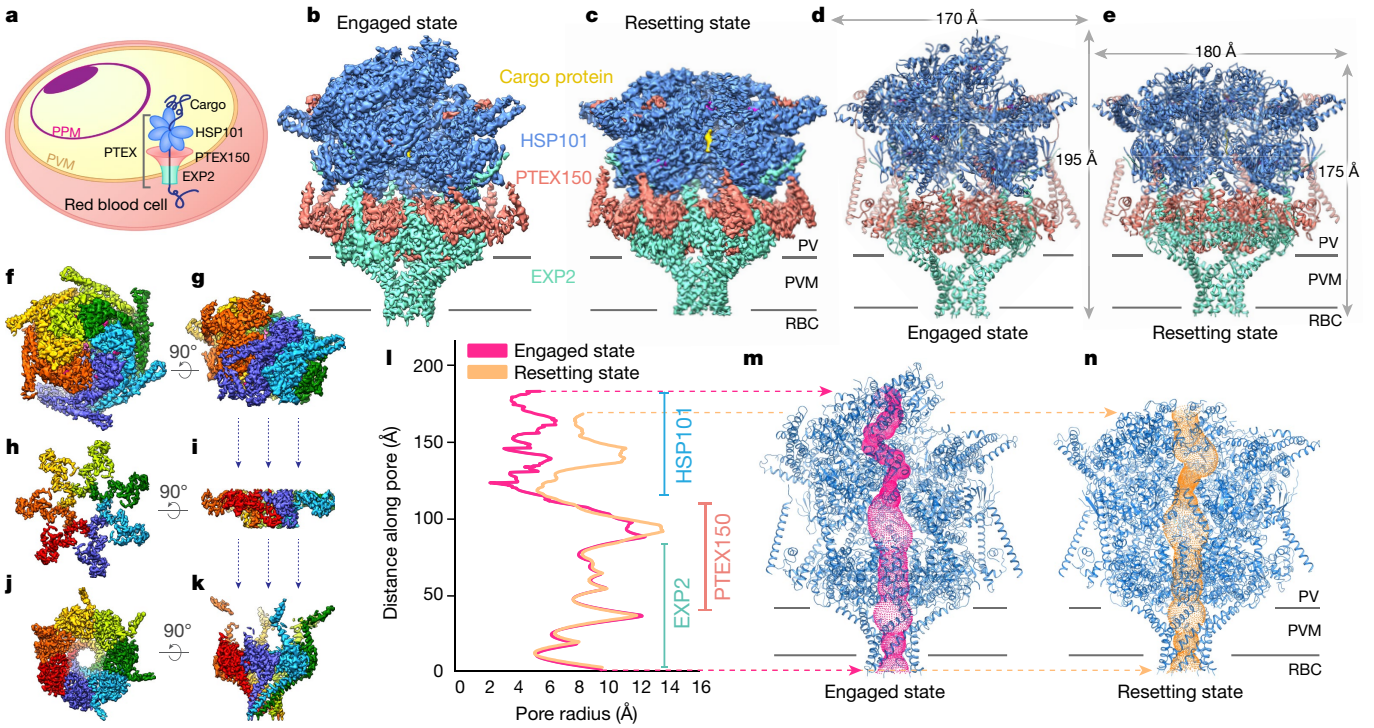

Fig. 1 | Global architecture of the PTEX core complex in two cargo-bound states. a, Schematic of a human erythrocyte infected with *P. falciparum*. PPM, parasite plasma membrane; PVM, parasitophorous vacuole membrane. **b**–**e**, Cryo-EM maps (**b**, **c**) and atomic models (**d**, **e**) of the PTEX core complex. Horizontal lines represent the PVM bilayer, estimated on the basis of the detergent belt density, which is visible at lower thresholds (see Extended Data Fig. 7). PV, parasitophorous vacuole; RBC, red blood cell. **f**–**k**, Top and side views of the HSP101 (**f**, **g**), PTEX150 (**h**, **i**) and EXP2 (**j**, **k**) cryo-EM maps, coloured by protomer. **l**–**n**, Pore radius (**l**) and protein-conducting channel (**m**, **n**) calculated using HOLE[40].

Both structures show that PTEX is a tripartite membrane protein complex with a 6:7:7 stoichiometry and a calculated mass of 1.6 MDa, composed of a hexameric HSP101 protein-unfolding motor tethered to a PVM-spanning, pseudosymmetric funnel formed by seven protomers of EXP2 interdigitating with seven protomers of PTEX150 (Fig. 1d–k, Supplementary Video 3). Two transiently associated[21] accessory proteins, PTEX88 and TRX2[14], are not seen in our structures. At the PVM, each EXP2 monomer contributes a single transmembrane helix to form a seven-fold (C7)-symmetric protein-conducting channel spanning the membrane (Fig. 1j, k). Six HSP101 protomers are tethered on top of the PTEX150–EXP2 funnel in a hexameric right-handed spiral, with a gap between the bottom-most and top-most protomers (Fig. 1f, g, Supplementary Video 4). The HSP101 hexamer is oriented such that a single unbroken channel extends from the top of the HSP101 hexamer to the bottom of the heptameric EXP2 transmembrane pore (Fig. 1l–n, Extended Data Fig. 2d). The most constricted point along the channel occurs in HSP101, measuring 4 Å and 10 Å in diameter in the engaged and resetting states, respectively (Fig. 1l). The seventh EXP2 and PTEX150 protomers are situated under the gap between HSP101 protomers 1 and 6, accommodating the remarkable symmetry mismatch between the asymmetric HSP101 hexamer and the pseudo-seven-fold-symmetric PTEX150–EXP2 tetradecamer (Fig. 1f–k, Extended Data Fig. 2e–j). Analyses of our PTEX150 and EXP2 structures with four commonly used structural similarity search programs[22–25] found no consistent structural similarities to any known proteins, including the pore-forming toxin haemolysin E, with which EXP2 was previously speculated to share structural homology[14]. Below, we describe the structural details of the individual proteins in the engaged state, followed by a comparison of the two states that suggests a mechanism of translocation.

EXP2 forms a protein-conducting channel across PVM

Residues G27–S234 of EXP2 are well-resolved in our structure, accounting for 80% of the mature protein (Extended Data Fig. 6a). EXP2 is a single-pass transmembrane protein consisting of a kinked 60 Å N-terminal transmembrane helix followed by a globular body domain and ending in an assembly domain composed of a linker helix followed by the assembly strand (Fig. 2a, b). The body domain contains five helices, B1–B5, which are stabilized by an intraprotomer C113–C140 disulphide bond (Fig. 2c).

Seven EXP2 protomers (which we labelled A–G) oligomerize to form a funnel-shaped C7-pseudosymmetric 216-kDa heptamer spanning the PVM (Fig. 2d, e). The transmembrane domain and body helices B1–B3 are symmetric throughout all seven protomers (Extended Data Fig. 3a, b). This symmetry is broken by inter-protomer conformational variations in body helices B4–B5 and the assembly domain, which stretch upwards in some protomers to maintain contacts with the asymmetric HSP101 hexamer located above the EXP2 funnel. This variation is most pronounced in EXP2 protomers F and G (Extended Data Fig. 3a, b).

In the EXP2 heptamer, the amphipathic transmembrane helices twist slightly around each other, creating a 37 Å-long C7-symmetric protein-conducting channel that spans the PVM and forms the stem of the funnel (Fig. 2d, e). The membrane-facing surface of the EXP2 channel is coated with hydrophobic residues, whereas the inner surface is lined with charged and polar residues, creating an aqueous pore (Fig. 2e). The body domains, positioned in a wider ring on top of the transmembrane channel on the vacuolar face of the PVM, form the mouth of the funnel. This orientation is consistent with previous analyses of EXP2 topology[14,20]. Furthermore, a detergent belt is clearly visible in 2D class averages and density maps (Extended Data Figs. 7, 8), defining the residues in the transmembrane domain that would be buried in the PVM. A ring of positively charged residues where the stem meets the mouth of the funnel is positioned where it can interact with the negatively charged phosphates of the membrane surface (Extended Data Fig. 8a).

PTEX150 forms an adaptor between HSP101 and EXP2

Of the 993 residues in PTEX150, S668–D823 are well-resolved in the structure, and form a hook with a shaft (Fig. 3a, b). The hook

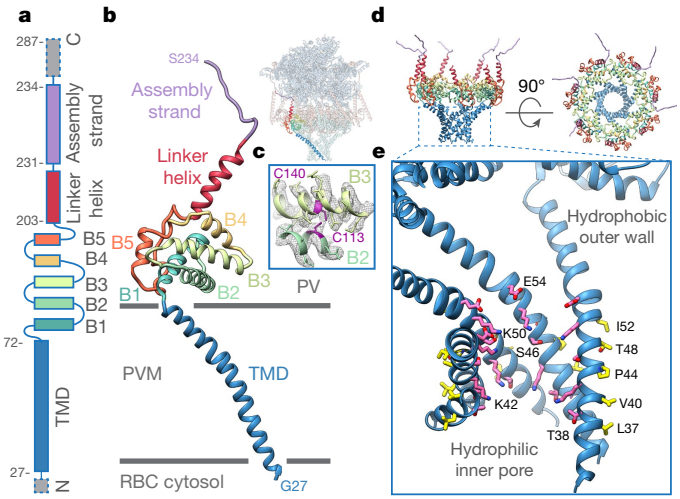

Fig. 2 | EXP2 forms a heptameric pseudo-symmetric PVM-spanning pore. a, **b**, Linear schematic (**a**) and ribbon diagram (**b**) of the EXP2 monomer in the engaged state. Dashed grey boxes represent unmodelled regions. Inset, one EXP2 monomer (coloured) within the PTEX complex. TMD, transmembrane domain. **c**, Density (mesh) and model of the C113–C140 disulphide bond. **d**, EXP2 heptamer, coloured as in **b**. **e**, Cutaway of the EXP2 transmembrane channel with hydrophilic residues (pink) lining the inner protein-conducting pore and hydrophobic residues (yellow) on the outer, membrane-facing surface.

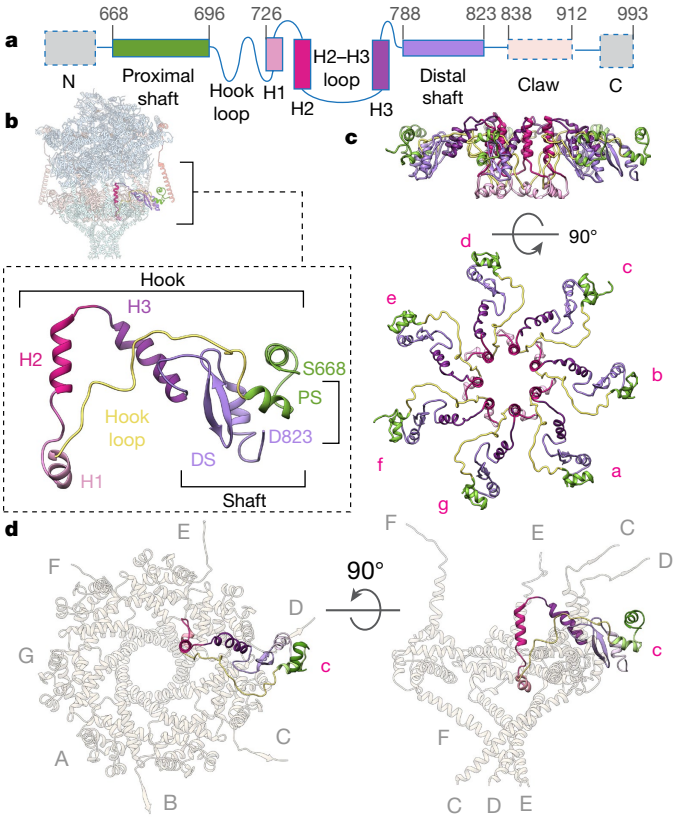

Fig. 3 | PTEX150 forms a heptameric flange-shaped adaptor between EXP2 and HSP101. a, **b**, Linear schematic (**a**) and ribbon diagram (**b**) of the PTEX150(668–823) monomer in the engaged state. Dashed grey boxes represent unmodelled regions. Inset, one PTEX150(668–823) monomer (coloured) within the PTEX complex. PS, proximal shaft; DS, distal shaft. **c**, The PTEX150(668–823) heptamer, coloured as in **b**. **d**, Views showing how one PTEX150(668–823) monomer hooks into the top of the EXP2 funnel.

domain consists of three short helices (H1–H3), which are connected by several long loops. Directly N-terminal and C-terminal to the hook domain, the shaft is composed of proximal and distal shaft domains (Fig. 3a, b). The remaining 80% of PTEX150—not visible in our structures—is predicted to be intrinsically disordered (in this region the average disorder tendency score in IUPred[26,27] is 0.83, with scores above 0.5 indicating disorder), unlike the rigid structured core of PTEX150(S668–D823) (with an average disorder tendency score of 0.42, indicating ordered structure), suggesting that this 80% of the protein is too mobile to be observed and may be flexibly arranged outside the stable PTEX core.

Seven PTEX150(S668–D823) hooks (which we labelled a–g) oligomerize, forming a flange-shaped C7-pseudosymmetric heptamer (Fig. 3c) that fits into the mouth of the EXP2 channel. Each hook lies in the groove between adjacent EXP2 body domains, and the tip of the hook curls down into the mouth of the EXP2 pore (Fig. 3d). A vertical, heptameric ring of H2 helices sits in the mouth of the EXP2 funnel, forming a conduit between the hexameric HSP101 and heptameric EXP2 central pores (Extended Data Fig. 2g–j). In this way, PTEX150(S668–D823) serves as an adaptor between HSP101 and EXP2, providing a continuous protected path for unfolded cargo.

Endogenous cargo is observed in the channel of HSP101

Class 1 Clp–HSP100 AAA+ ATPases are highly conserved hexameric protein unfoldases that are associated with diverse functions; they are known to thread polymeric substrates through a central pore[28,29]. HSP101 is a 598-kDa hexamer, exemplifying the canonical class 1 Clp–HSP100 domain architecture[30,31], with a substrate-binding N-terminal domain[32] followed by two AAA+ nucleotide-binding domains (NBD1 and NBD2), each containing a cargo-binding pore loop (L1 and L2, respectively) that extends into the central pore (Fig. 4a, b). Additionally, HSP101 contains a C-terminal domain and a coiled-coil middle domain insertion in the C-terminal end of NBD1 (Fig. 4a, b).

Unlike class 2 HSP100s [33], class 1 HSP100s form three-tiered hexamers, in which the N-terminal domains, NBD1s and NBD2s form the top, middle and bottom tiers, respectively[30,31]. In our engaged state structure, the NBD1 and NBD2 tiers are arranged in a right-handed ascending spiral[30,31,34] (Fig. 4c). A layer of weaker density above the NBD1 tier may correspond to the N-terminal domains, which are likely to be dynamic (Extended Data Fig. 8b). The middle domains encircle the upper NBD1 tier. The central pore of the spiral is lined with pore loops bearing tyrosines in a spiral staircase pattern. The tyrosine sidechain densities intercalate with a 45 Å-long density that is clearly visible in the middle of the chaperone pore (Fig. 4c, d, Supplementary Video 5), which closely resembles unfolded cargo polypeptide densities reported in recently published cryo-EM structures of homologous HSP100s bound to cargo[31,33] (Extended Data Fig. 2a, d). The unfolded PTEX cargo polypeptide chain modelled into this 45 Å density matches very closely (root mean square deviation (r.m.s.d.) of 1.09–1.25 Å) with the unfolded cargo polypeptides in these cargo-bound homologue structures (Extended Data Fig. 2a–c).

Key interactions for PTEX assembly and function

The three PTEX components share extensive binding interfaces; here we describe the two most noteworthy interactions. In each EXP2 protomer A–F, the assembly strand augments the C-terminal domain β-sheet in the HSP101 protomer situated directly above it (Fig. 5a, b). Protomer G occupies the space below the gap between HSP101 protomers 1 and 6 (Fig. 1f–k). This hydrogen bond interaction tethers the HSP101 hexamer to the transmembrane funnel, positioning the central pore exit directly above the entrance to the PTEX150–EXP2 pore. We hypothesized that this interaction is essential for assembly of the PTEX core complex, and that the complex must be stably assembled to be active. We tested this using genetic functional complementation in live *P. falciparum*.

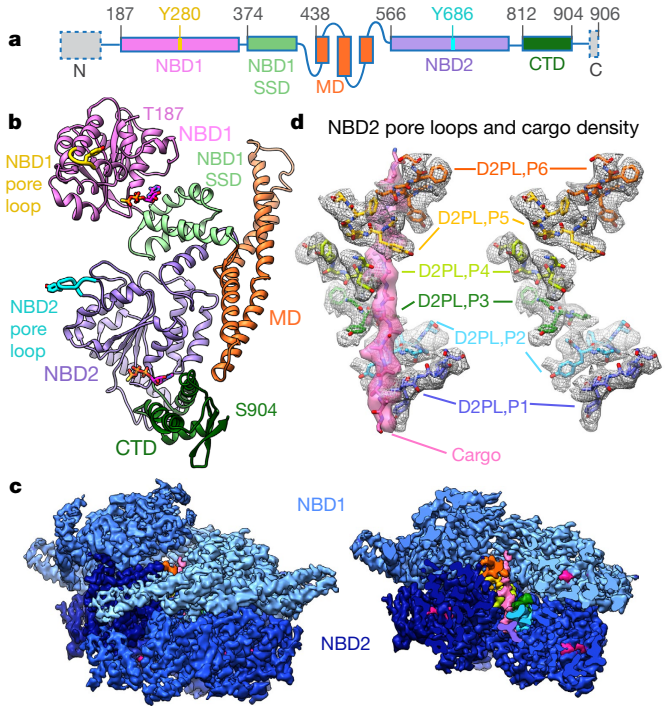

Fig. 4 | Endogenous cargo bound in the channel of the HSP101 hexamer. a, **b**, Linear schematic (**a**) and ribbon diagram (**b**) of the HSP101 monomer in the engaged state. MD, middle domain; CTD, C-terminal domain. SSD, small subdomain. **c**, Side view of the full (left) and bisected (right) cryo-EM map of the HSP101 hexamer. NBD1 and NBD2 rings are coloured with light (NBD1) and dark (NBD2) blue gradients to emphasize the right-handed spiral shape of the hexamer. The bisected map shows NBD2 pore loop densities coloured by protomer, ATPγS (magenta) and the cargo density (light pink). **d**, Enlarged side view of the atomic models of the HSP101 NBD2 pore loops and unfolded cargo polypeptide backbone, shown with densities. NBD2 pore loops are coloured as in **c** and labelled by protomer (for example, D2PL,P1 is NBD2 pore loop, protomer 1). Vertical distances between pore loop tyrosines in D2PL,P1–D2PL,P6 are 6.52 Å, 6.28 Å, 6.38 Å, 6.96 Å and 6.12 Å, respectively.

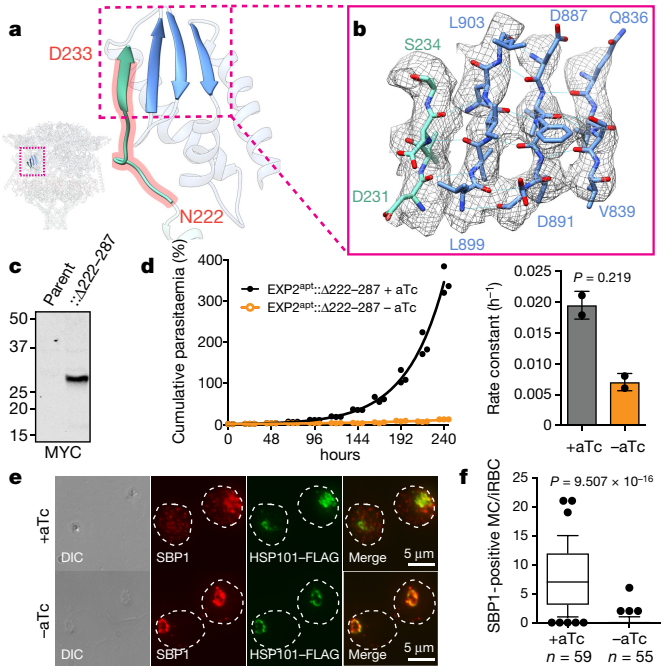

Fig. 5 | Interactions essential for PTEX function. a, **b**, Ribbon (**a**) and stick (**b**) models of the HSP101 C-terminal domain β-sheet augmented by the EXP2 assembly strand, shown with corresponding cryo-EM density (mesh). The segment outlined in red was truncated in functional complementation assays. **c**, Western blot of lysates from *P. falciparum* expressing EXP2 under aptamer control (EXP2^{apt}) complemented with EXP2(Δ222–287)–3×Myc (predicted molecular weight 27.8 kDa after signal peptide cleavage). For blot source data, see Supplementary Fig. 1. **d**, Growth analysis of EXP2^{apt}::EXP2(Δ222–287)–3×Myc. *P. falciparum* were grown with or without anhydrotetracycline (aTc) to maintain or knockdown endogenous EXP2 expression, respectively. One experiment performed with three technical replicates is shown. Bars show mean exponential growth rate constant (h^{-1}) determined from the fit of the two independent experiments and error bars indicate s.d. **e**, Immunofluorescence assay detecting exported protein SBP1 and HSP101–3×FLAG (a marker of the parasitophorous vacuole) in *P. falciparum* expressing EXP2^{apt}::EXP2(Δ222–287)–3×Myc that were allowed to develop with or without aTc for 24 h after invasion. The dashed line indicates the traced boundary of the red blood cell. DIC, differential interference contrast image. **f**, Quantification of SBP1 export immunofluorescence assays. Data are pooled from two independent experiments; *n* is the number of individual parasite-infected RBCs. Boxes and whiskers delineate 25th to 75th and 10th to 90th percentiles, respectively. All *P* values are determined by an unpaired, two-sided Student's *t*-test. All data shown represent two independent experiments.

Knockdown of EXP2 produces a lethal defect in *P. falciparum* growth and export that can be rescued by a mutant version of EXP2 that lacks the C-terminal 54 residues[20]. Therefore, the amino acids immediately following the assembly strand are not essential for PTEX function. However, complementation with a version of EXP2 that lacks an additional 12 residues, removing the assembly strand, failed to rescue these phenotypes (Fig. 5c–f). These results demonstrate that the EXP2 assembly strand is critical to PTEX function, consistent with an essential role for it in docking the HSP101 unfoldase to the EXP2 membrane channel to facilitate translocation.

A strong, albeit lower resolution claw-shaped density extends from the end of each modelled PTEX150(S668–D832) shaft to the HSP101 middle domain above, terminating in a three-turn helix that rests on the midpoint of the middle domain. This helix forms a strong interaction with Y488 and Y491 of HSP101 in claws a–e (Extended Data Fig. 8d–e), but is not visible in claw f in the engaged state. Claw g appears to form an additional interaction with the N-terminal end of the middle domain of HSP101 protomer 1 (Extended Data Fig. 8d). The middle domain is known to have a critical role in regulating ATPase and unfoldase activities in related HSP100s[35,36], suggesting that this interaction is of high functional importance.

Two observed states suggest a translocation mechanism

In addition to the extended 195 Å engaged state of PTEX, we also observed a more compact 175 Å resetting state. Much of PTEX150(S668–D823) and EXP2 remain unchanged between the engaged and resetting states; a hinge-like swinging motion in the HSP101 hexamer accounts for the 20 Å difference in height. The transmembrane domain and B1–B3 helices of EXP2 exhibit C7 symmetry, and remain identical between the two states (Supplementary Video 6). The deviations from C7 symmetry in the B4–B5 helices and assembly domain are less pronounced in the resetting state (Extended Data Fig. 3b, c), probably owing to the more planar arrangement of HSP101 protomers. As in the engaged state, slight inter-protomer variations in the H2–H3 region of PTEX150(S668–D823) bridge the gap between EXP2 and HSP101, maintaining a continuous protected path for unfolded cargo proteins.

The spiral staircase of HSP101 tyrosine pore loops in the engaged state collapses into a planar C shape in the resetting state (Supplementary Video 7), with a freedom of movement possibly conferred by the gap between HSP101 protomers 1 and 6[30,31]. Starting at the interface between the NBD2 domains of HSP101 protomers 3 and 4, HSP101 protomers 4–6 swing downwards and outwards, creating a deep vertical cleft through the central pore of the hexamer.

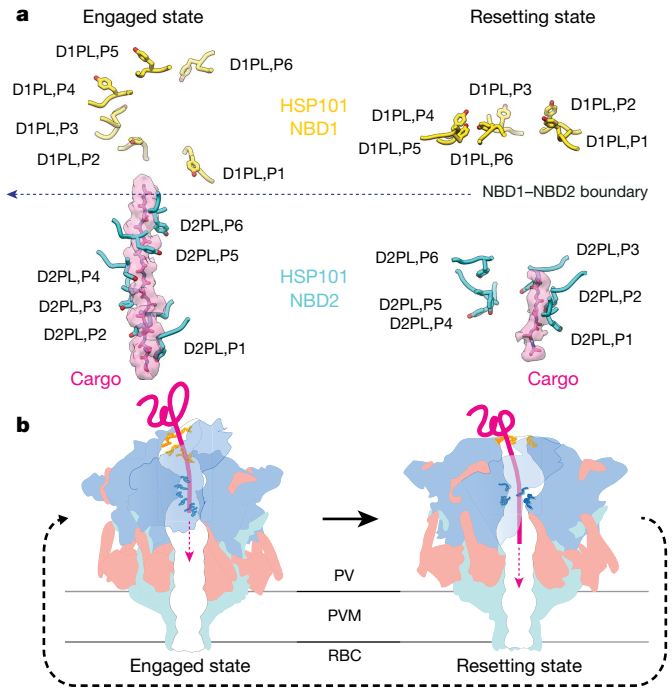

Fig. 6 | Mechanism of translocation. a, Side views of the HSP101 pore loops with the unfolded cargo peptide backbone models (dark pink) built into the cryo-EM densities (light pink). Vertical distances between pore loop tyrosines in consecutive loops are as follows. Engaged D1PL,P1–D1PL,P6: 9.41 Å, 8.61 Å, 1.40 Å, 3.34 Å and 2.28 Å, respectively. Engaged D2PL,P1–D2PL,P6: 6.52 Å, 6.28 Å, 6.38 Å, 6.96 Å and 6.12Å, respectively. Resetting D1PL,P1–D1PL,P6: 1.75 Å, −2.70 Å, −1.65 Å, −0.78 Å and 1.81 Å, respectively. Resetting D2PL,P1–D2PL,P6: 5.88 Å, 4.56 Å, −6.80 Å, 2.25 Å and 7.88 Å, respectively. **b**, Proposed stepwise feeding mechanism of translocation by PTEX. NBD1 and NBD2 pore loops and cargo are coloured as in **a**.

This movement pulls the NBD2 loops in protomers 4–6 away from the unfolded cargo (Extended Data Fig. 3d, e, h, i, Supplementary Videos 6, 7). A shorter (19 Å versus 45 Å), unfolded cargo density remains visible, bound to the NBD2 loops in protomers 1–3, whereas no peptide density is visible in protomers 4–6 (Fig. 6a, Extended Data Fig. 3h, i). Furthermore, the NBD1 domain of protomer 3 rotates outward, such that the R361 arginine finger remains within 5.2 Å of the ATPγS bound to NBD1 of protomer 4, and the nucleotide in NBD2 of protomer 4 shifts 7.5 Å away from the R859 arginine finger in protomer 3 (Extended Data Fig. 3f, g).

Discussion

We propose a PTEX-mediated mechanism of protein translocation via a cyclic process involving at least two discrete states (Fig. 6b, Supplementary Videos 6, 7), which we have captured by purifying PTEX complexes directly from *P. falciparum* that are actively translocating cargo. The pore loops in HSP101 NBD2 form two 'hands' that work together to thread the cargo protein through the central pore. NBD2 loops from HSP101 protomers 1–3 form the passive hand, located closest to the PTEX150(S668–D823)–EXP2 funnel, which remains fixed between states (Fig. 6a, b). NBD2 loops from HSP101 protomers 4–6 form the active hand, which moves along the channel axis (above the passive hand), grasping the unfolding peptide and feeding it through the passive hand. In the engaged state, all six NBD2 pore loops grip the unfolded peptide in the spiral staircase formation (Fig. 6a, b). As the HSP101 hexamer collapses into the resetting state, the active hand moves downwards, feeding the newly unfolded peptide through the passive hand, into the PTEX150(S668–D823)–EXP2 funnel below. The passive hand then grips the unfolded peptide, preventing it from slipping back towards the HSP101 apical entrance while the active hand swings outward, releasing the cargo (Fig. 6a, b). Finally, the active hand moves upwards to grasp the unfolding protein further upstream, transitioning back to the engaged state. This cyclic feeding mechanism threads the unfolded cargo protein through the translocon, across the PVM and into the cytosol of the host cell.

The states captured here may be two of several states in the processive phase of translocation. Additional states are likely to exist for cargo recognition. Although we did not observe PTEX-free HSP101 oligomers as has been suggested[37], we did observe additional, seemingly cargo-free PTEX complexes (Extended Data Fig. 9) that did not refine to better than 7 Å, suggesting that there is conformational heterogeneity in the absence of stabilizing cargo interactions. Cargo–PTEX interactions during cargo recognition may be transient, possibly explaining why we did not observe the N-terminal domains of HSP101, or other components that are potentially required for cargo recognition. Without these details, the mechanisms of cargo recognition and subsequent refolding after translocation remain unclear, although there is some evidence for the involvement of exported parasite chaperones[38] or co-opted host chaperonins[39] in these processes. Of note, on the basis of secondary structure prediction and PTEX150 truncation experiments[37], PTEX150 residues D838–F912 may occupy the claw (PTEX150 residues D838–E873) and three-turn helix (PTEX150 residues S884–F912) densities that remain unassigned in our structures.

Our work demonstrates the advantages of obtaining structures of challenging protein complexes in functionally relevant states by imaging samples purified directly from endogenous sources. Direct observation of the native PTEX core provides compelling evidence that this complex containing EXP2, PTEX150 and HSP101 is a bona fide translocon that is embedded in the PVM and serves as the gateway for the malaria parasite exportome. In addition to establishing the role of EXP2 as the membrane-spanning pore of PTEX and providing insight into the mechanism of this essential protein translocating machine, our structures reveal an interaction between the EXP2 assembly domain and the C-terminal domain of HSP101 that is indispensable for PTEX function. These atomic structures of PTEX provide potential targets for designing a new class of drugs to inhibit this essential gatekeeper of the malarial exportome.

Online content

Any methods, additional references, Nature Research reporting summaries, source data, statements of data availability and associated accession codes are available at https://doi.org/10.1038/s41586-018-0469-4.

Received: 29 March 2018; Accepted: 19 July 2018;
Published online 27 August 2018.

1. World Health Organization. *World Malaria Report 2017*. (World Health Organization, Geneva, 2017).
2. Miller, L. H., Ackerman, H. C., Su, X. Z. & Wellems, T. E. Malaria biology and disease pathogenesis: insights for new treatments. *Nat. Med.* **19**, 156–167 (2013).
3. Cowman, A. F., Healer, J., Marapana, D. & Marsh, K. Malaria: biology and disease. *Cell* **167**, 610–624 (2016).
4. Spillman, N. J., Beck, J. R. & Goldberg, D. E. Protein export into malaria parasite-infected erythrocytes: mechanisms and functional consequences. *Annu. Rev. Biochem.* **84**, 813–841 (2015).
5. Boddey, J. A. & Cowman, A. F. *Plasmodium* nesting: remaking the erythrocyte from the inside out. *Annu. Rev. Microbiol.* **67**, 243–269 (2013).
6. Przyborski, J. M., Nyboer, B. & Lanzer, M. Ticket to ride: export of proteins to the *Plasmodium falciparum*-infected erythrocyte. *Mol. Microbiol.* **101**, 1–11 (2016).
7. de Koning-Ward, T. F., Dixon, M. W., Tilley, L. & Gilson, P. R. *Plasmodium* species: master renovators of their host cells. *Nat. Rev. Microbiol.* **14**, 494–507 (2016).
8. Marti, M., Good, R. T., Rug, M., Knuepfer, E. & Cowman, A. F. Targeting malaria virulence and remodeling proteins to the host erythrocyte. *Science* **306**, 1930–1933 (2004).
9. Hiller, N. L. et al. A host-targeting signal in virulence proteins reveals a secretome in malarial infection. *Science* **306**, 1934–1937 (2004).
10. Heiber, A. et al. Identification of new PNEPs indicates a substantial non-PEXEL exportome and underpins common features in *Plasmodium falciparum* protein export. *PLoS Pathog.* **9**, e1003546 (2013).
11. Lingelbach, K. & Joiner, K. A. The parasitophorous vacuole membrane surrounding *Plasmodium* and *Toxoplasma*: an unusual compartment in infected cells. *J. Cell Sci.* **111**, 1467–1475 (1998).

12. Ansorge, I., Benting, J., Bhakdi, S. & Lingelbach, K. Protein sorting in *Plasmodium falciparum*-infected red blood cells permeabilized with the pore-forming protein streptolysin O. *Biochem. J.* **315**, 307–314 (1996).
13. Gehde, N. et al. Protein unfolding is an essential requirement for transport across the parasitophorous vacuolar membrane of *Plasmodium falciparum*. *Mol. Microbiol.* **71**, 613–628 (2009).
14. de Koning-Ward, T. F. et al. A newly discovered protein export machine in malaria parasites. *Nature* **459**, 945–949 (2009).
15. Beck, J. R., Muralidharan, V., Oksman, A. & Goldberg, D. E. PTEX component HSP101 mediates export of diverse malaria effectors into host erythrocytes. *Nature* **511**, 592–595 (2014).
16. Elsworth, B. et al. PTEX is an essential nexus for protein export in malaria parasites. *Nature* **511**, 587–591 (2014).
17. Bullen, H. E. et al. Biosynthesis, localization, and macromolecular arrangement of the *Plasmodium falciparum* translocon of exported proteins (PTEX). *J. Biol. Chem.* **287**, 7871–7884 (2012).
18. Johnson, D. et al. Characterization of membrane proteins exported from *Plasmodium falciparum* into the host erythrocyte. *Parasitology* **109**, 1–9 (1994).
19. Gold, D. A. et al. The *Toxoplasma* dense granule proteins GRA17 and GRA23 mediate the movement of small molecules between the host and the parasitophorous vacuole. *Cell Host Microbe* **17**, 642–652 (2015).
20. Garten, M. et al. R. EXP2 is a nutrient-permeable channel in the vacuolar membrane of *Plasmodium* and is essential for protein export via PTEX. *Nat. Microbiol.* https://doi.org/10.1038/s41564-018-0222-7 (2018).
21. Chisholm, S. A. et al. The malaria PTEX component PTEX88 interacts most closely with HSP101 at the host-parasite interface. *FEBS J.* **285**, 2037–2055 (2018).
22. Holm, L. & Laakso, L. M. Dali server update. *Nucleic Acids Res.* **44**, W351–W355 (2016).
23. Gibrat, J. F., Madej, T. & Bryant, S. H. Surprising similarities in structure comparison. *Curr. Opin. Struct. Biol.* **6**, 377–385 (1996).
24. Wiederstein, M., Gruber, M., Frank, K., Melo, F. & Sippl, M. J. Structure-based characterization of multiprotein complexes. *Structure* **22**, 1063–1070 (2014).
25. Krissinel, E. & Henrick, K. Secondary-structure matching (SSM), a new tool for fast protein structure alignment in three dimensions. *Acta Crystallogr. D Biol. Crystallogr.* **60**, 2256–2268 (2004).
26. Dosztanyi, Z., Csizmok, V., Tompa, P. & Simon, I. IUPred: web server for the prediction of intrinsically unstructured regions of proteins based on estimated energy content. *Bioinformatics* **21**, 3433–3434 (2005).
27. Dosztanyi, Z., Csizmok, V., Tompa, P. & Simon, I. The pairwise energy content estimated from amino acid composition discriminates between folded and intrinsically unstructured proteins. *J. Mol. Biol.* **347**, 827–839 (2005).
28. Schirmer, E. C., Glover, J. R., Singer, M. A. & Lindquist, S. HSP100/Clp proteins: A common mechanism explains diverse functions. *Trends Biochem. Sci.* **21**, 289–296 (1996).
29. Hanson, P. I. & Whiteheart, S. W. AAA+ proteins: have engine, will work. *Nat. Rev. Mol. Cell Biol.* **6**, 519–529 (2005).
30. Deville, C. et al. Structural pathway of regulated substrate transfer and threading through an Hsp100 disaggregase. *Sci. Adv.* **3**, e1701726 (2017).
31. Gates, S. N. et al. Ratchet-like polypeptide translocation mechanism of the AAA+ disaggregase Hsp104. *Science* **357**, 273–279 (2017).
32. AhYoung. A. P., Koehl, A., Cascio, D. & Egea, P. F. Structural mapping of the ClpB ATPases of *Plasmodium falciparum*: targeting protein folding and secretion for antimalarial drug design. *Protein Sci.* **24**, 1508–1520 (2015).
33. Puchades, C. et al. Structure of the mitochondrial inner membrane AAA+ protease YME1 gives insight into substrate processing. *Science* **358**, (2017).
34. Yokom, A. L. et al. Spiral architecture of the Hsp104 disaggregase reveals the basis for polypeptide translocation. *Nat. Struct. Mol. Biol.* **23**, 830–837 (2016).
35. Seyffer, F. et al. Hsp70 proteins bind Hsp100 regulatory M domains to activate AAA+ disaggregase at aggregate surfaces. *Nat. Struct. Mol. Biol.* **19**, 1347–1355 (2012).
36. Lipinska, N. et al. Disruption of ionic interactions between the nucleotide binding domain 1 (NBD1) and middle (M) domain in Hsp100 disaggregase unleashes toxic hyperactivity and partial independence from Hsp70. *J. Biol. Chem.* **288**, 2857–2869 (2013).
37. Elsworth, B. et al. Proteomic analysis reveals novel proteins associated with the *Plasmodium* protein exporter PTEX and a loss of complex stability upon truncation of the core PTEX component, PTEX150. *Cell. Microbiol.* **18**, 1551–1569 (2016).
38. Kulzer, S. et al. *Plasmodium falciparum*-encoded exported hsp70–hsp40 chaperonen–co-chaperone complexes within the host erythrocyte. *Cell. Microbiol.* **14**, 1784–1795 (2012).
39. Batinovic, S. et al. An exported protein-interacting complex involved in the trafficking of virulence determinants in *Plasmodium*-infected erythrocytes. *Nat. Commun.* **8**, 16044 (2017).
40. Smart, O. S., Neduvelil, J. G., Wang, X., Wallace, B. A. & Sansom, M. S. P. HOLE: A program for the analysis of the pore dimensions of ion channel structural models. *J. Mol. Graph.* **14**, 354–360 (1996).

Acknowledgements This research was supported in part by grants from National Institutes of Health (R21AI125983 to P.F.E., R01GM071940/AI094386/DE025567 to Z.H.Z. and K99/R00 HL133453 to J.R.B.). P.F.E. is the Alexander and Renee Kolin Endowed Chair in Molecular Biology and Biophysics. C.-M.H. acknowledges funding from the Ruth L. Kirschstein National Research Service Award (AI007323). We thank the UCLA Proteome Research Center for assistance in mass spectrometry and acknowledge the use of instruments in the Electron Imaging Center for Nanomachines supported by UCLA and grants from NIH (S10RR23057, S10OD018111 and U24GM116792) and NSF (DBI-1338135 and DMR-1548924). We thank A. W. P. Fitzpatrick for input on cryo-EM aspects of the project and J. Su for helping with Fig. 1a.

Reviewer information *Nature* thanks A. Cowman, P. da Fonseca and W. Hol for their contribution to the peer review of this work.

Author contributions C.-M.H., P.F.E. and Z.H.Z. initiated the project; J.R.B. generated *P. falciparum* lines, collected *P. falciparum*, performed complementation experiments and helped to write the paper; C.-M.H. purified the sample, screened purified samples by negative stain, prepared cryo-EM grids, acquired and processed the cryo-EM data, interpreted the structures and wrote the paper; M.L. built and refined the atomic models and helped to interpret the structures; Y.C. helped with sample freezing; Z.H.Z. supervised the cryo-EM aspects of the project, interpreted the structures and wrote the paper; P.F.E. supervised biochemical aspects of the project and helped to interpret the structures; D.E.G. supervised parasitology aspects of the project. D.E.G., M.L. and P.F.E. helped to edit the paper. Queries regarding cryo-EM and atomic modelling should be addressed to Z.H.Z. and queries on biochemistry should be addressed to P.F.E.

Competing interests The authors declare no competing interests.

Additional information

Extended data is available for this paper at https://doi.org/10.1038/s41586-018-0469-4.
Supplementary information is available for this paper at https://doi.org/10.1038/s41586-018-0469-4.

Correspondence and requests for materials should be addressed to P.F.E. or Z.H.Z.

METHODS

No statistical methods were used to predetermine sample size. The experiments were not randomized. The investigators were not blinded to allocation during experiments and outcome assessment.

Cells. *P. falciparum* strain NF54^{attB} was obtained from the Fidock laboratory where it was generated[41] and was used exclusively in the study. De-identified, IRB-exempt expired RBCs were obtained from the blood bank at the St. Louis Children's Hospital. PCR amplified regions from the NF54^{attB} genome were found to match the genome sequence for 3D7, a sub clone of NF54. The presence of the cg6 localized attB sequence was verified by successful Bxb1-mediated integration at that site. Cell lines were not tested for mycoplasma contamination.

***P. falciparum* culture and genetic modification for PTEX purification.** *P. falciparum* culture was performed as described[42] with the exception that RPMI was supplemented with 0.5% Albumax I. All plasmid construction was carried out by infusion cloning (Clontech) unless otherwise noted. Integration of a 3×Flag fusion at the endogenous HSP101 C terminus was accomplished with CRISPR–Cas9 editing. A Cas9 target site was chosen just upstream of the *hsp101* stop codon (TAATAGTAAAGCTAAAAACT) and the guide RNA seed sequence was synthesized as a sense and anti-sense primer pair (sense shown) 5′-TAAGTATATAATATTTAATAGTAAAGCTAAAAACTGTTTTAGAGCTAGAA-3′, annealed and inserted into the BtgZI site of the plasmid pAIO[43], resulting in the plasmid pAIO-HSP101-CT-gRNA1. A 5′-homology flank (up to but not including the stop codon) was amplified from *P. falciparum* NF54^{attB} genomic DNA using primers 5′-GACGCGAGGAAAATTAGCATGCATCCTTAAGGAGATTCTGGTATGCCACTTGGTTC-3′ and 5′-CTGCACCTGGCCTAGGGGTCTTAGATAAGTTTATAACTAAGTTTTTAGCTTTACTATT-3′, incorporating a synonymous shield mutation in the protospacer adjustment motif of the gRNA target site within the *hsp101* coding sequence. A 3′-homology flank (beginning 3 bp downstream of the stop codon) was amplified using primers 5′-CACTATAGAACTCGAGAATTACGCATATATATATATATATATATATATATAACATGGGTTG-3′ and 5′-GAACCAAGTGGCATACCAGAATCTCCTTAAGGATGCATGCTAATTTTCCTCGCGTC-3′. The flank amplicons were assembled in a second PCR reaction using primers 5′-CACTATAGAACTCGAGAATTACGCATATATATATATATATATATATATAACATGGGTTG-3′ and 5′-CTGCACCTGGCCTAGGGGTCTTAGATAAGTTTATAACTAAGTTTTTAGCTTTACTATT-3′ and inserted between XhoI and AvrII in pPM2GT[42]. The GFP tag between AvrII and EagI in this vector was then replaced with sequence encoding a 3×Flag tag using the primer 5′-CTTAGTTATAAACTTATCTAAGACCCCTAGGGACTACAAGGACGACGACGACAAGGATTATAAAGATGATGATGATAAAGATTATAAAGATGATGATGATAAATGACGGCCGCGTCGAGTTATATAATATATTTATG-3′ and a QuikChange Lightning Multi Site-Directed Mutagenesis kit (Agilent), resulting in the plasmid pPM2GT-HSP101-3×Flag. This plasmid was linearized at the AflII site between the 3′ and 5′-homology flanks and co-transfected with pAIO-HSP101-CT-gRNA1 into *P. falciparum* NF54^{attB} parasites[41]. Selection with 10 nM WR99210 was applied 24 h after transfection. Once *P. falciparum* returned from selection, integration at the intended site was confirmed by PCR with primers 5′-CGAAAACTTTTATGGTATTAATATAACAG-3′ and 5′-CCTTGTCGTCGTCGTCCTTG-3′ and a clonal line was isolated by limiting dilution.

For PTEX purification, *P. falciparum* expressing HSP101-3×Flag were synchronized by serial treatment with 5% w/v D-sorbitol and then expanded while shaking to increase singlet invasion events and maintain synchrony. For each preparation, ~2×10^{10} erythrocytes infected with *P. falciparum* were collected at the ring stage (typically ~500 ml 2% haematocrit culture at ~20% parasitaemia). Erythrocytes were lysed in 10× pellet volume of cold phosphate-buffered saline (PBS) containing 0.0125% saponin (Sigma, sapogenin content ≥ 10%) and EDTA-free protease inhibitor cocktail (Roche or Pierce). Released *P. falciparum* were washed in cold PBS containing EDTA-free protease inhibitor cocktail and washed cell pellets were frozen in liquid nitrogen and stored at −80 °C.

Affinity purification of PTEX core complex from *P. falciparum* pellets. Frozen *P. falciparum* pellets were resuspended in lysis buffer (25 mM HEPES pH 7.4, 10 mM $MgCl_2$, 150 mM KCl, 10% glycerol) and homogenized using a glass Dounce tissue homogenizer. The membrane fraction was isolated from the homogenized lysate by centrifugation at 100,000*g* for 1 h. The membrane pellet was solubilized in solubilization buffer (25 mM HEPES pH 7.4, 10 mM $MgCl_2$, 150 mM KCl, 10% glycerol, 0.4% triton X-100) and the solubilized membranes were then applied to anti-Flag M2 affinity gel resin (Sigma). The resin was washed extensively in wash buffer (25 mM HEPES pH 7.4, 10 mM $MgCl_2$, 150 mM KCl, 10% glycerol, 0.015% triton X-100), after which the protein was eluted from the affinity resin with elution buffer (25 mM HEPES pH 7.4, 10 mM $MgCl_2$, 150 mM KCl, 2 mM ATPγS, 0.015% triton X-100, 500 μg/ml Flag peptide).

The presence and relative abundance of the three PTEX core components were verified by silver stained SDS–PAGE and tryptic digest liquid chromatography–mass spectrometry (Extended Data Fig. 1e, f). The extremely low yields achievable when purifying PTEX directly from *P. falciparum* prohibited the conventional approach of evaluating sample quality by size exclusion chromatography. Thus, during the iterative process of screening for optimal purification conditions, sample quality was assessed by negative stain (uranyl acetate) transmission electron microscopy in an FEI TF20 microscope equipped with a TVIPS 16 mega-pixel CCD camera. In brief, small datasets of ~100,000 particles were collected and 2D class averages were generated in RELION[44,45] to assess the presence of sufficient numbers of intact PTEX particles yielding 'good' class averages exhibiting distinct features. For example, C7 symmetry could be recognized in top views, and the characteristic Clp/HSP100 layers were visible in side views (Extended Data Fig. 6a–c).

Cryo-electron microscopy. Three-microlitre aliquots of purified PTEX core complex were applied to glow-discharged lacey carbon grids with a supporting ultrathin carbon film (Ted Pella). Grids were then blotted with filter paper and vitrified in liquid ethane using an FEI Vitrobot Mark IV or a home-made manual plunger. Cryo-EM grids were screened in an FEI Tecnai TF20 transmission electron microscope while optimizing freezing conditions.

Higher resolution cryo-EM images were collected on a Gatan K2-Summit direct electron detector in counting mode on an FEI Titan Krios at 300 kV equipped with a Gatan Quantum energy filter set at a 20 eV slit width. Fifty frames were recorded for each movie at a pixel size of 1.04 Å at the specimen scale, with a 200-ms exposure time and an average dose rate of 1.2 electrons per $Å^2$ per frame, resulting in a total dose of 60 electrons per $Å^2$ per movie. The final dataset consists of a total of 25,000 movies recorded in four separate sessions.

Image processing and 3D reconstruction. Frames in each movie were aligned, gain reference-corrected and dose-weighted to generate a micrograph using MotionCor2[46]. Aligned and un-dose-weighted micrographs were also generated and used for contrast transfer function (CTF) estimation using CTFFIND4[47] and PTEX particle picking by hand and using Gautomatch (https://www.mrc-lmb.cam.ac.uk/kzhang/Gautomatch/Gautomatch_Brief_Manual.pdf).

In total, 1,508,462 particles were extracted from 19,752 micrographs and initially binned by a factor of 2. After two rounds of reference-free two-dimensional (2D) classification in RELION, 422,713 particles were selected as 'good' particles from distinct 2D class averages representing different views of the PTEX core complex. These particles were then used in a one-class ab initio reconstruction followed by homogeneous refinement in CryoSPARC[48], yielding a 4.8 Å ab initio 3D map.

The original 422,713 'good' particles were then aligned in a 3D refinement in RELION using the 4.8 Å CryoSPARC map as an initial reference. All subsequent image-processing steps were performed using RELION. After this refinement, the particles were unbinned, their centres recalculated and used to re-extract particles from the original micrographs without binning. The newly extracted, unbinned particles were then aligned with a second 3D refinement yielding a ~4.5 Å reconstruction.

An exhaustive, iterative search of classification and refinement conditions was used to sort out different conformations and further improve resolution (Extended Data Fig. 9). In brief, upon further sorting using 3D-classification without alignment, we identified two homogenous particle subsets corresponding to the engaged and resetting states (Extended Data Fig. 9). Particles in the two subsets were refined separately, yielding full maps with overall resolutions of 4.16 Å and 4.23 Å, respectively.

Focused 3D classification without alignment followed by focused refinement was used to further improve the resolution of mobile regions of the structure in both states. C7 symmetry was applied in the focused 3D classification and refinement steps of the heptameric halves, comprising EXP2 and PTEX150, yielding a 3.4 Å engaged state map and a 3.5 Å resetting state map (Extended Data Figs. 3, 9). The same procedure, except with C1 symmetry, was applied to the hexameric half of the engaged state, yielding a 4.09 Å map (Extended Data Figs. 3, 9). This last step was also applied to the hexameric half of the resetting state, but did not yield improvements in resolution. Further efforts of focused 3D classification and refinement of individual HSP101 protomers, individual claws, and HSP101 N-terminal domain densities in the two states did not ultimately yield improvements in resolution in either state.

Model building and refinement. Map interpretation was performed with UCSF Chimera[49] and COOT[50]. *P. falciparum* protein sequences were obtained from the National Center for Biotechnology Information (NCBI)[51] and the PlasmoDB[52] protein databases. PHYRE2[53] secondary structure predictions were used as an aid for initial manual sequence registration. Models for a single monomer of HSP101, PTEX150, and EXP2 in the engaged state were all built de novo. This first model for each protein monomer was then placed into the density maps of other protomers to aid de novo modelling of subsequent protomers. Individual protomers in the complex were then manually remodelled to ensure a close fit between densities and models. The same process was repeated for the resetting state. Manual refinement targeting protein geometry alone was done primarily along the periphery and flexible regions of the complex (for example, the M domains of HSP101). Whereas

their densities and backbone traces were visible, we were unable to model the claw with its connected three-turn helix, nor one of the 12 M domain loops in the resetting state (Fig. 5g, h). The three-turn helix displayed a few bulky side chains interacting with the M domain of HSP101; however, the lack of backbone connection to our atomic model of the complex and the limited visibility of smaller side chains in this region made sequence assignment challenging.

Manual refinement targeting both protein geometry and fit with the density map was used primarily in the core regions where resolution was higher and noise was minimal. Rotamers were fitted manually in COOT and improved using the 'back-rub rotamers' setting. The resulting models for the complexes were subjected to the phenix.real_space_refine program in PHENIX[54]. Following this step, Molprobity[55] reported less than ideal clash scores and map-to-model cross-correlation. To improve the geometry and fit, manual adjustments were made to protein geometry and density map fit, with the additional step of using Molprobity[55] clash dots and sphere-refinement in COOT.

The complex was then broken into three portions: (1) symmetric regions of EXP2 and PTEX150, (2) HSP101, and (3) the full PTEX complex. These model segments were fed back to phenix.geometry_minimization in PHENIX and then to phenix.real_space_refine using simulated annealing and global minimization applying Emsley's Ramachandran restraints[50]. Following another round of manual checks and improvements, all models were subjected to phenix.real_space_refine with default settings one last time.

All figures and videos were prepared with UCSF Chimera, Pymol (https://www.pymol.org), and Resmap[56]. Molprobity was used to validate the stereochemistry of the final models.

Genetic complementation. For expression of a complementing second copy of truncated EXP2, the *exp2* coding sequence up to codon position 221 was amplified with primers 5′-CGAATAAACACGATTTTTTCTCGAGATGAAAGTCAGTTATATATTTTCCTTTTTTTTGTTATTCTTCG-3′ and 5′-AATCAACTTTTGTTCGCTAGCTTTCTTTGATTCCATAGATTTCAATTTCTCTTCC-3′ and inserted into the plasmid pyEOE-attP-EXP2-3×Myc[20] between XhoI and NheI, resulting in the plasmid pyEOE-attP-EXP2Δ222-287-3×Myc. This plasmid was co-transfected with pINT[41] into EXP2^{apt}::HSP101-3×Flag conditional knockdown parasites[20] at the mature schizont stage using a Nucleofector 2b and Basic Parasite Nucleofector kit 2 (Lonza). Selection with 2 μM DSM1[57] was applied 24 h post-transfection (in addition to 2.5 μg/ml blasticidin S and 1 μM anhydrotetracycline for maintenance of endogenous EXP2 translational control by the aptamer system) to facilitate integration into the attP site engineered in the benign *cg6* locus through integrase mediated attB × attP recombination. Following return from selection, *P. falciparum* were cloned by limiting dilution, and expression of EXP2(Δ222–287)–3×Myc was confirmed by western blot.

***P. falciparum* growth assays.** EXP2^{apt}::EXP2(Δ222–287) *P. falciparum* were extensively washed to remove aTc and plated with or without 1 μM aTc in triplicate at an initial parasitaemia of 1%. The medium was changed every 48 h and 1:1 subculture was performed every other day beginning on day 4 to avoid culture overgrowth. Parasitaemia (percentage of total red blood cells (RBCs) infected) was measured every 24 h by flow cytometry on a FACSCanto (BD Biosciences) by nucleic acid staining of cultured RBCs with PBS containing 0.8 μg/ml acridine orange. Cumulative parasitaemias were back calculated based on the subculture schedule and data were fitted to an exponential growth equation to determine rate constants using Prism (Graphpad).

Quantification of protein export. For evaluation of protein export by immunofluorescence assay (IFA), mature schizonts were purified on a magnetic column and allowed to invade fresh, uninfected RBCs with shaking for 3 h before treatment with 5% w/v D-sorbitol to destroy unruptured schizonts. Pulse-invaded cells were plated with or without 1 μM aTc and allowed to develop 24 h post-invasion. Thin smears of infected RBCs were briefly air dried and immediately fixed in ice-cold acetone for 2 min. After fixation, samples were blocked for 30 min in PBS + 3% BSA followed by incubation for 1 h with primary antibody solutions containing mouse anti-Flag M2 monoclonal antibody (detecting HSP101–3×Flag to mark the PVM) and rabbit anti-SBP1. After washing, secondary antibody incubation was carried out for 1 h with Alexa Fluor anti-mouse 488 and anti-rabbit 594 IgG antibodies (Life Technologies), each diluted 1:2,000. After final washing, coverslips were mounted over each sample using Pro-long antifade Gold with DAPI (Life Technologies). Images were collected with an ORCA-ER CCD camera (Hamamatsu) using AxioVision software on an Axio Imager.M1 microscope (Zeiss) with a 100× oil-immersion objective using the same exposure times for each image (300 ms for SBP1-594, 150 ms for Flag-488). Ten images were acquired for each condition using the DAPI channel for field selection to avoid bias. Images were then analysed using Volocity 6.3 (PerkinElmer). The border of each single-infected erythrocyte was traced using the DIC channel as a guide to define a region of interest (ROI). The PVM was marked using the 'find objects' measurement tool for the HSP101–3×Flag–488 channel (automatic threshold setting with threshold offset set to −30% and minimum object size set to 0.5 μm^2). Individual Maurer's clefts were identified using the 'find spots' measurement tool for the SBP1-594 channel (offset minimum spot intensity set to 40% and brightest spot within radius set to 0.5 μm). All spots within the PVM object boundary were then removed using the 'subtract' measurement tool and the number and fluorescent intensity of the remaining spots in each ROI were collected. Data were pooled from two independent experiments and plotted with Prism.

Antibodies. The following primary antibodies were used for IFA and western blot: mouse anti-Flag monoclonal antibody clone M2 (Sigma) (IFA, 1:500; western blot, 1:500); rabbit polyclonal anti-SBP1[58] (IFA, 1:500); mouse anti-cMYC monoclonal antibody 9E10 (ThermoFisher) (western blot, 1:300).

Reporting summary. Further information on research design is available in the Nature Research Reporting Summary linked to this paper.

Data availability. The atomic models have been deposited to the Protein Data Bank under accession numbers 6E10 and 6E11 and the cryo-EM density maps have been deposited in the Electron Microscopy Data Bank under accession numbers EMD-8951 and EMD-8952.

41. Adjalley, S. H. et al. Quantitative assessment of *Plasmodium falciparum* sexual development reveals potent transmission-blocking activity by methylene blue. *Proc. Natl Acad. Sci. USA* **108**, E1214–E1223 (2011).
42. Klemba, M., Beatty, W., Gluzman, I. & Goldberg, D. E. Trafficking of plasmepsin II to the food vacuole of the malaria parasite *Plasmodium falciparum*. *J. Cell Biol.* **164**, 47–56 (2004).
43. Spillman, N. J., Beck, J. R., Ganesan, S. M., Niles, J. C. & Goldberg, D. E. The chaperonin TRiC forms an oligomeric complex in the malaria parasite cytosol. *Cell Microbiol.* **19**, e12719 (2017).
44. Scheres, S. H. W. A Bayesian view on cryo-EM structure determination. *J. Mol. Biol.* **415**, 406–418 (2012).
45. Scheres, S. H. W. RELION: implementation of a Bayesian approach to cryo-EM structure determination. *J. Struct. Biol.* **180**, 519–530 (2012).
46. Zheng, S. Q. et al. MotionCor2: anisotropic correction of beam-induced motion for improved cryo-electron microscopy. *Nat. Methods* **14**, 331–332 (2017).
47. Rohou, A. & Grigorieff, N. CTFFIND4: fast and accurate defocus estimation from electron micrographs. *J. Struct. Biol.* **192**, 216–221 (2015).
48. Punjani, A., Rubinstein, J. L., Fleet, D. J. & Brubaker, M. A. cryoSPARC: algorithms for rapid unsupervised cryo-EM structure determination. *Nat. Methods* **14**, 290–296 (2015).
49. Pettersen, E. F. et al. UCSF chimera—a visualization system for exploratory research and analysis. *J. Comput. Chem.* **25**, 1605–1612 (2004).
50. Emsley, P., Lohkamp, B., Scott, W. G. & Cowtan, K. Features and development of Coot. *Acta Crystallogr. D* **66**, 486–501 (2010).
51. NCBI Resource Coordinators. Database resources of the National Center for Biotechnology Information. *Nucleic Acids Res.* **44**, D7–D19 (2016).
52. Aurrecoechea, C. et al. PlasmoDB: a functional genomic database for malaria parasites. *Nucleic Acids Res.* **37**, D539–D543 (2009).
53. Kelley, L. A., Mezulis, S., Yates, C. M., Wass, M. N. & Sternberg, M. J. E. The Phyre2 web portal for protein modeling, prediction and analysis. *Nat. Protoc.* **10**, 845–858 (2015).
54. Adams, P. D. et al. PHENIX: a comprehensive Python-based system for macromolecular structure solution. *Acta Crystallogr. D* **66**, 213–221 (2010).
55. Chen, V. B. et al. MolProbity: all-atom structure validation for macromolecular crystallography. *Acta Crystallogr. D* **66**, 12–21 (2010).
56. Kucukelbir, A., Sigworth, F. J. & Tagare, H. D. Quantifying the local resolution of cryo-EMEM density maps. *Nat. Methods* **11**, 63–65 (2014).
57. Ganesan, S. M. et al. Yeast dihydroorotate dehydrogenase as a new selectable marker for *Plasmodium falciparum* transfection. *Mol. Biochem. Parasitol.* **177**, 29–34 (2011).
58. Blisnick, T. et al. Pfsbp 1, a Maurer's cleft *Plasmodium falciparum* protein, is associated with the erythrocyte skeleton. *Mol. Biochem. Parasitol.* **111**, 107–121 (2000).
59. Puchades, C. et al. Structure of the mitochondrial inner membrane AAA+ protease YME1 gives insight into substrate processing. *Science* **358**, eaao0464 (2017).

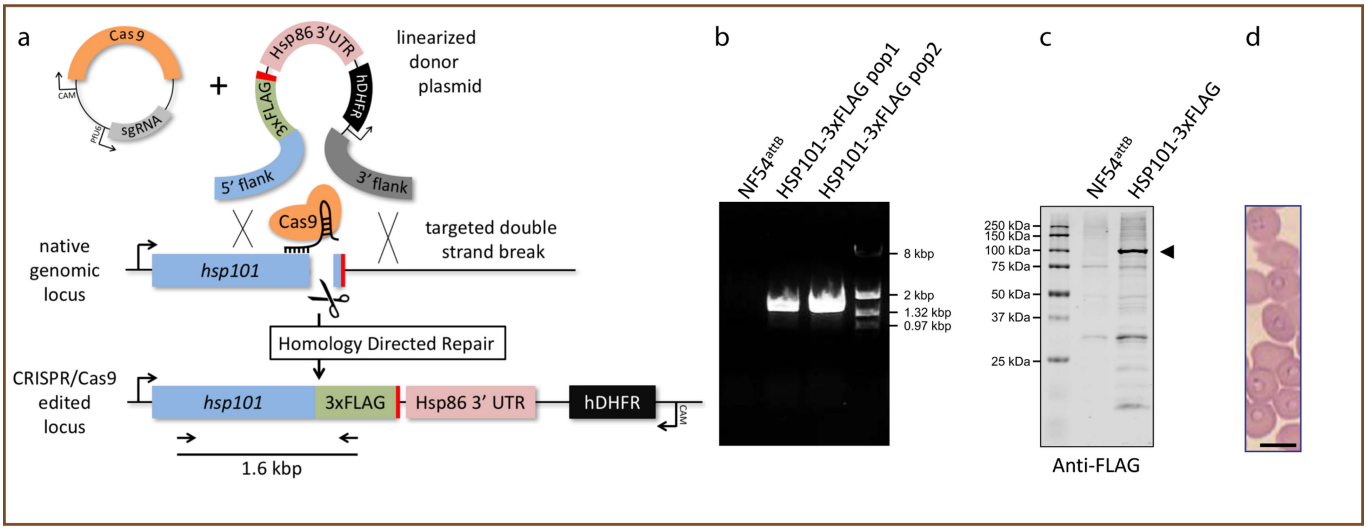

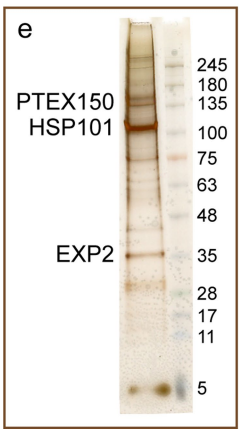

f

	Accession	Seq coverage	Seq count	Spec count	NSAF	EMPAI	Description
1	PF3D7_1116800	55.5	72	228	0.0750967	2.5892193	product=heat shock protein 101 (HSP101)
2	PF3D7_0917900	48.3	44	101	0.04622617	2.040885	product=heat shock protein 70 (HSP70-2)
3	PF3D7_1436300	58	58	135	0.04056941	2.8018937	product=translocon component PTEX150 (PTEX150)
4	PF3D7_1471100	40.8	13	34	0.03535177	1.5585859	product=exported protein 2 (EXP2)
5	PF3D7_1006200	59.8	7	7	0.019522185	2.9627802	product=DNA/RNA-binding protein Alba 3 (ALBA3)

Extended Data Fig. 1 | Generation of HSP101–3×Flag *P. falciparum* and analysis of purified PTEX. a, Schematic showing strategy for endogenous tagging of *P. falciparum hsp101* with 3×Flag using CRISPR–Cas9 editing. Diagnostic PCR primers and expected amplicon following successful integration are shown. sgRNA, single-guide RNA; UTR, untranslated region; CAM, calmodulin promoter; PfU6, *P. falciparum* U6 promoter; hDHFR, human dihydrofolate reductase. **b**, Diagnostic PCR with genomic DNA template from NF54^{attB} parent or two independent populations of HSP101–3×Flag *P. falciparum*. The experiment was performed once. **c**, Western blot of NF54^{attB} and HSP101–3×Flag *P. falciparum* probed with mouse Flag M2 antibody (Sigma) and goat anti-mouse IRDye 680 secondary antibody (Li-Cor). Arrowhead indicates full-length HSP101–3×Flag (predicted molecular weight 102.9 kDa after signal peptide cleavage). Data represent two independent experiments. **d**, Giemsa staining of parasite-infected human erythrocytes from which PTEX was purified. Scale bar, 5 μm. For source data, see Supplementary Fig. 3. **e**, Silver-stained SDS–PAGE of the Flag-purified PTEX sample. Identities of the bands labelled EXP2, PTEX150 and HSP101 were confirmed by tryptic digest liquid chromatography–mass spectrometry (LC–MS). **f**, Tryptic digest LC–MS analysis of the Flag-purified PTEX sample. The PTEX core components are among the five most abundant species detected in the purified sample. For gel and blot source data, see Supplementary Fig. 1.

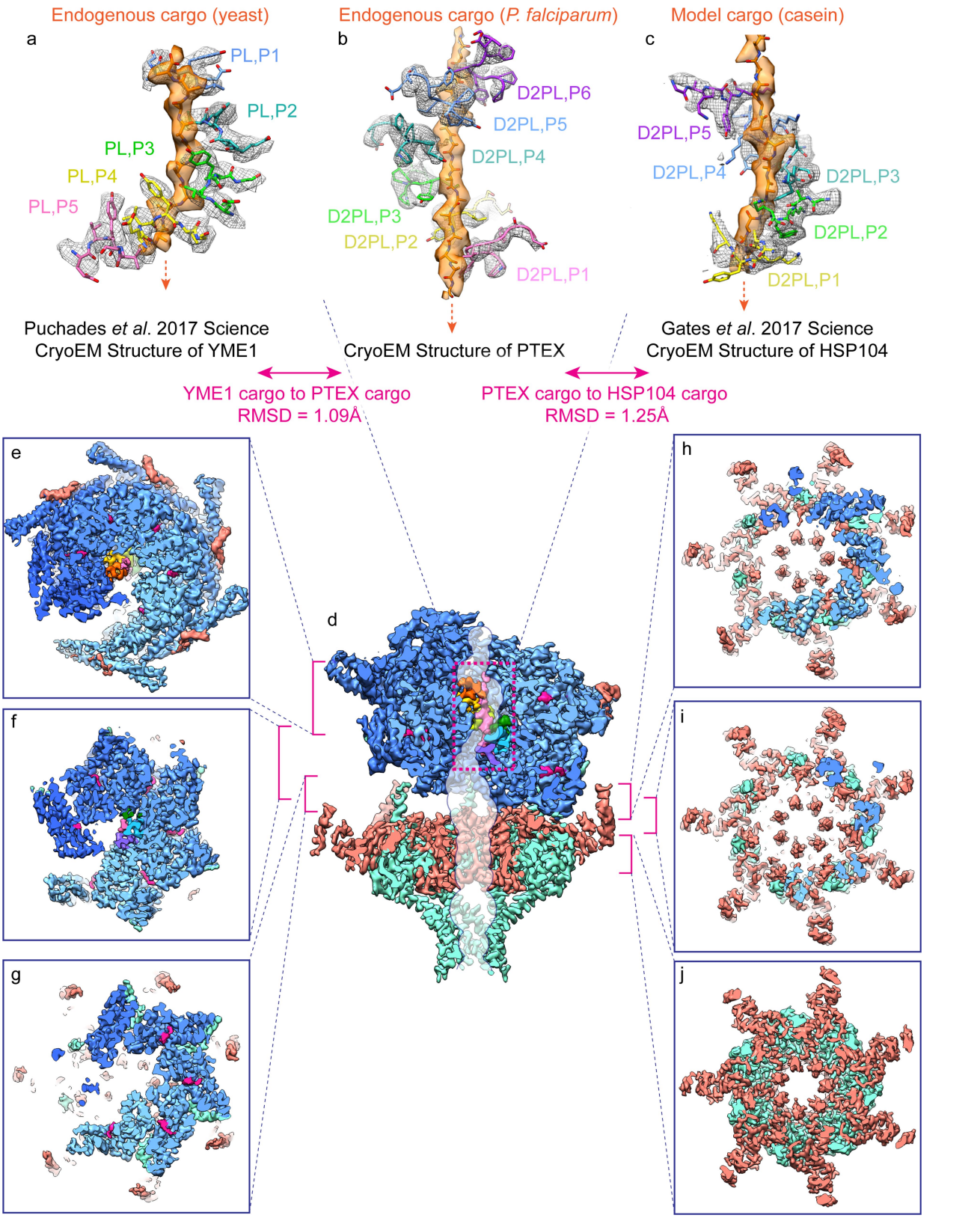

Extended Data Fig. 2 | See next page for caption.

Extended Data Fig. 2 | Detailed views of the PTEX protein-conducting channel and symmetry mismatch in the engaged state. a–c, Cryo-EM densities and atomic models of cargo and pore loops from the near-atomic resolution structures of Clp/HSP100 ATPases YME1[59] (**a**), PTEX HSP101 (**b**) and HSP104[31] (**c**). Tyrosine sidechain densities are clearly visibly intercalating with the cargo densities. The modelled engaged state PTEX cargo has a calculated r.m.s.d. of 1.09 Å and 1.25 Å to the published YME1 and HSP104 cargo models, respectively. Pore loops are labelled by NBD and protomer (for example, D2PL,P1 is NBD2 pore loop, protomer 1). **d**, Side view of the bisected engaged state PTEX cryo-EM map. The protein-conducting channel, calculated using HOLE[40], is shown superimposed over the bisected map in translucent white with a navy outline. The HSP101 NBD2 pore loop densities are coloured by HSP101 protomer, and the cargo density is coloured pink. **e–j**, The transition from the asymmetric HSP101 spiral to the C7-pseudosymmetric PTEX150(668–823)–EXP2 heptamer is depicted using a series of cross-sections taken perpendicular to the central axis of the translocon, spanning the area of symmetry mismatch. The section of the translocon corresponding to each cross-sectional image is indicated with a bracket in **d**.

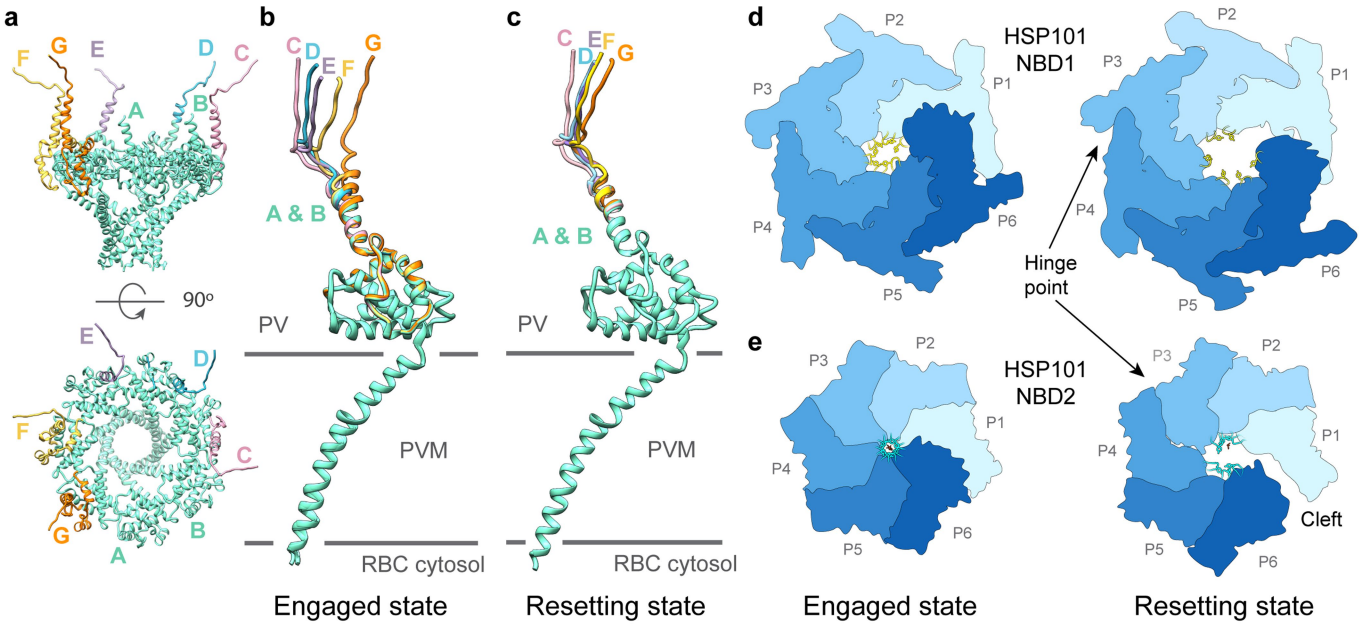

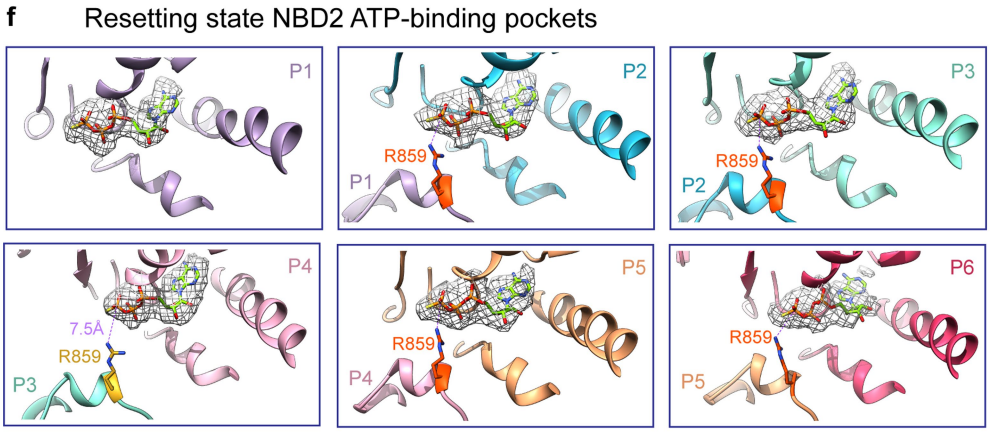

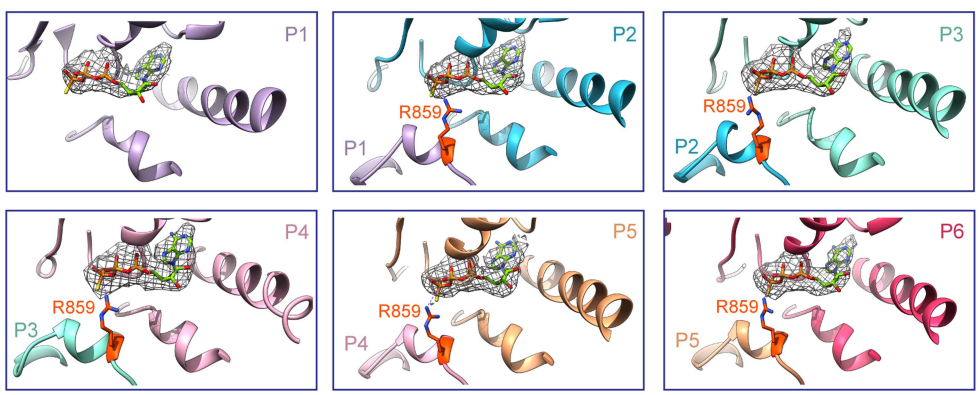

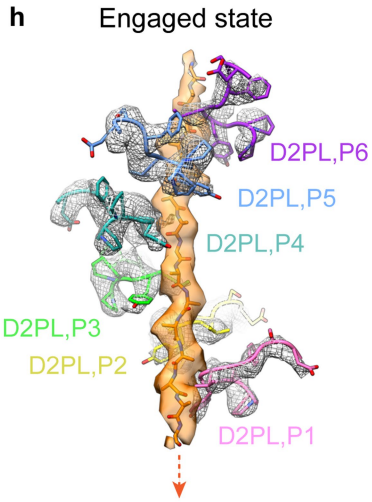

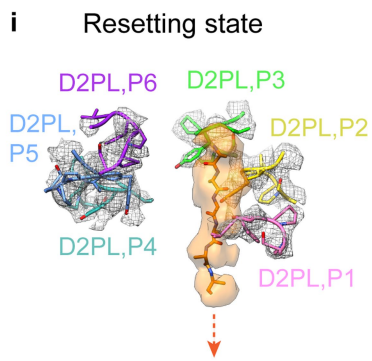

Extended Data Fig. 3 | See next page for caption.

Extended Data Fig. 3 | Detailed comparisons of the engaged and resetting states. a, Side and top views of the EXP2 heptamer in the engaged state. Symmetric portions that remain constant between protomers are coloured in mint. Portions that vary between protomers are coloured and labelled by protomer. **b**, **c**, Superposition of the seven EXP2 protomers, labelled A–G, in the engaged (**b**) and resetting (**c**) states, coloured as in **a**. **d**, **e**, Top view of HSP101 NBD1 (**d**) and NBD2 (**e**) in the engaged and resetting states, shown in simplified surface representation. The hinge point at the interface between HSP101 protomers 3 and 4 is indicated. **f**, **g**, Ribbon diagrams of the resetting state (**f**) and engaged state (**g**) nucleotide binding pockets are shown for each protomer. ATPγS in each pocket is shown with corresponding cryo-EM density (mesh). The R859 arginine finger (sidechain shown in red-orange) is positioned approximately 3–5.5 Å from the phosphorus atom in the γ-phosphate of the ATPγS in the binding pocket of the neighbouring protomer in all protomers except R859 in protomer 3 in the resetting state (sidechain shown in gold), where the ATPγS bound in the protomer 4 NBD2 nucleotide pocket has shifted approximately 7.5 Å away from the protomer 3 R859 arginine finger. **h**, **i**, Enlarged side view of the atomic models of the HSP101 NBD2 pore loops and unfolded cargo polypeptide backbone in the engaged (**h**) and resetting (**i**) states, shown with corresponding cryo-EM densities. Tyrosine sidechain densities are clearly visibly intercalating with the cargo densities. The modelled PTEX cargo has a calculated r.m.s.d. of 1.09 Å and 1.25 Å to the published YME1 and HSP104 cargo models, respectively. Pore loops are labelled by NBD and protomer (for example, D2PL,P1 is NBD2 pore loop, protomer 1).

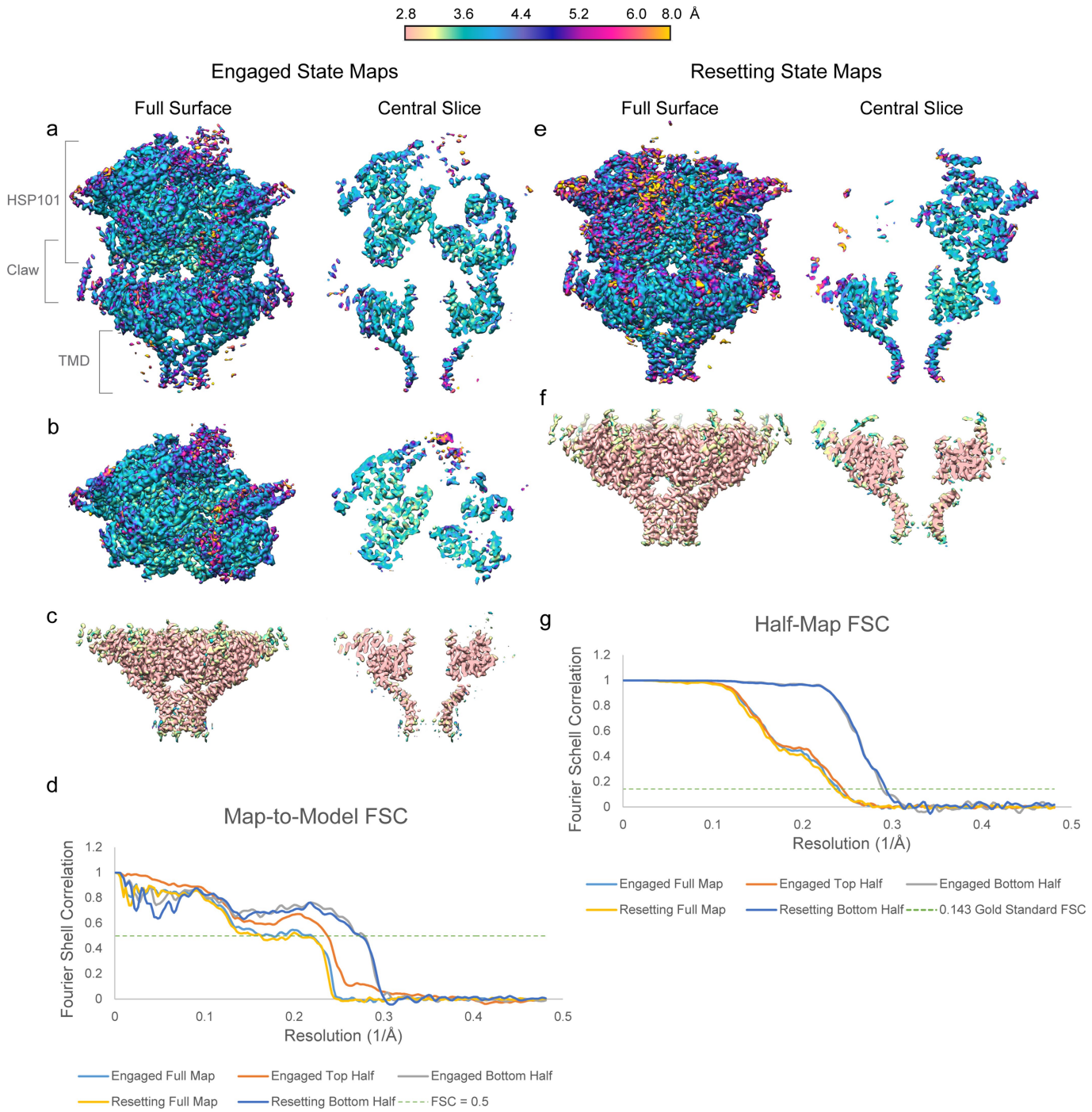

Extended Data Fig. 4 | Resolution assessments of the two PTEX states. **a**–**c**, **e**, **f**, Local resolution evaluations of the full PTEX map (**a**) and the focus-refined maps of the upper/hexameric (**b**) and lower/heptameric (**c**) halves of PTEX in the engaged state, the full PTEX map (**e**) and the focus-refined map of the lower/heptameric (**f**) half of PTEX in the resetting state, calculated by Resmap[56] and coloured according to resolution. Maps are displayed at higher thresholds where the detergent belt is not visible for clarity, to avoid obscuring details of the transmembrane helices. **d**, Global resolution assessment of the engaged and resetting state maps as measured using the 'Gold-standard' Fourier shell correlation (FSC) curves generated by RELION[44,45] by comparison of two independently refined 'half-maps'. **g**, Map-to-model FSC curves demonstrating the degree of correlation between the refined PTEX models and the experimental cryo-EM maps for the engaged and resetting states.

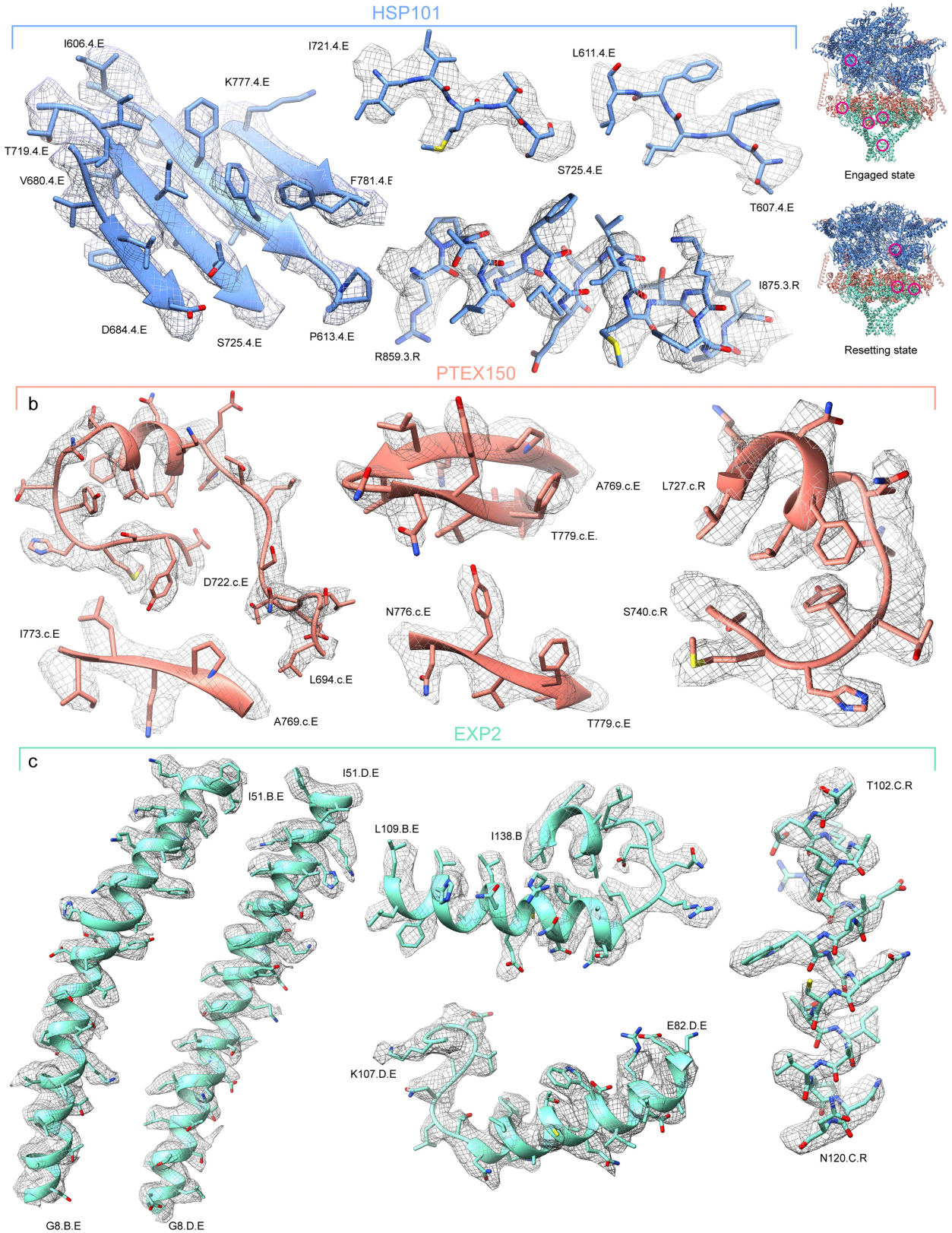

Extended Data Fig. 5 | Representative regions of cryo-EM density and atomic models. Additional cryo-EM densities (mesh) superposed with our atomic models for HSP101 (**a**), PTEX150(668–823) (**b**) and EXP2 (**c**). Displayed regions correspond to areas circled in magenta on guide figures (inset, upper right), and are coloured as in the guide figure: HSP101 (cornflower blue), PTEX150(668-823) (salmon), EXP2 (mint). Terminal residues for each segment are labelled with the amino acid, residue number, protomer, and state.

Extended Data Fig. 6 | See next page for caption.

Extended Data Fig. 6 | Experimentally determined secondary structure elements and detected mass-spectrometry fragments mapped to the primary sequences of the three PTEX proteins. For EXP2 (**a**), PTEX150 (**b**) and HSP101 (**c**), secondary structure elements are shown as tubes (helices), lines (loops), and arrows (strands) above the corresponding sequence and are coloured as in Figs. 2a, 3a, 4a. In the sequences shown below, residues resolved in our structures are coloured according to protein colours in Fig. 1c–f: EXP2 (mint), PTEX150 (salmon) and HSP101 (cornflower). Signal peptide residues are coloured gold. All residues in the mature proteins that are not resolved in our structures are shown in grey. The 3×Flag residues at the C terminus of HSP101 are coloured green. Peptides detected in tryptic digest liquid chromatography–tandem mass spectrometry (LC–MS/MS) analysis of the purified PTEX sample are shown as black lines below the corresponding sequences. Arrowheads above the EXP2 sequence indicate truncations sites described in this work and previously[20] immediately before (Δ222–287, red arrowhead) and after (Δ234–287, green arrowhead) the assembly strand. Arrowheads above the PTEX150 sequence indicate previously described truncation sites[37] (Δ847–993, red arrowhead; Δ869–993, green arrowhead).

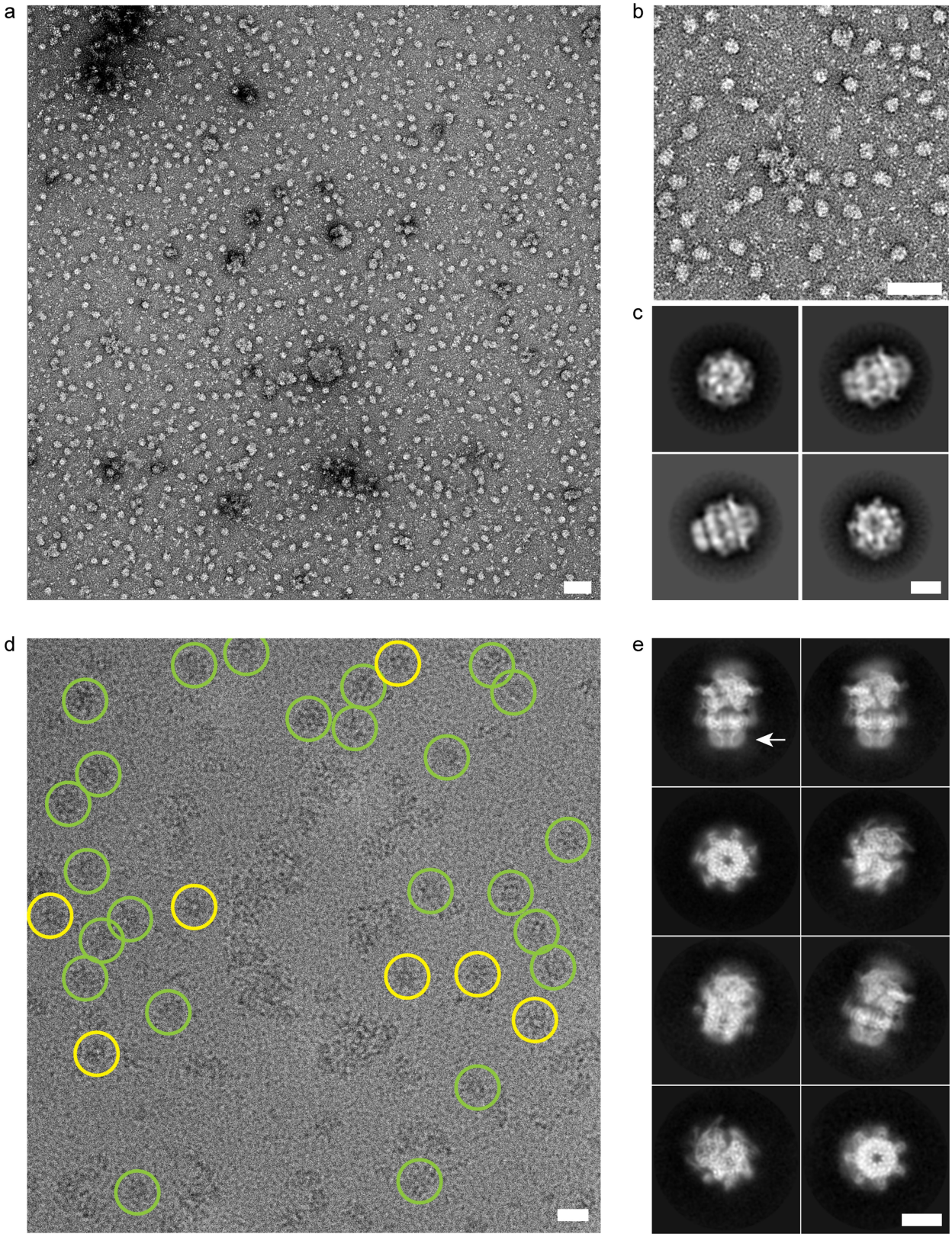

Extended Data Fig. 7 | Electron microscopy of the PTEX core complex. **a**–**c**, Representative negative stain micrograph (**a**), enlarged portion of micrograph (**b**) and two-dimensional class averages (**c**) of the PTEX core complex in multiple orientations. **d**, **e**, Representative cryo-EM micrograph (**d**) and two-dimensional class averages (**e**) of the PTEX core complex in multiple orientations. Individual particles in **d** are circled in yellow (top views) and green (side and oblique views) (for source data, see Supplementary Fig. 4). Arrow in upper left panel of **e** indicates the detergent belt, which is visible as a less-dense (dimmer) halo surrounding the denser (brighter) densities of the α-helices visible in the transmembrane domain in side views. Scale bars: 700 Å (**a**), 700 Å (**b**), 100 Å (**c**), 200 Å (**d**) and 100 Å (**e**).

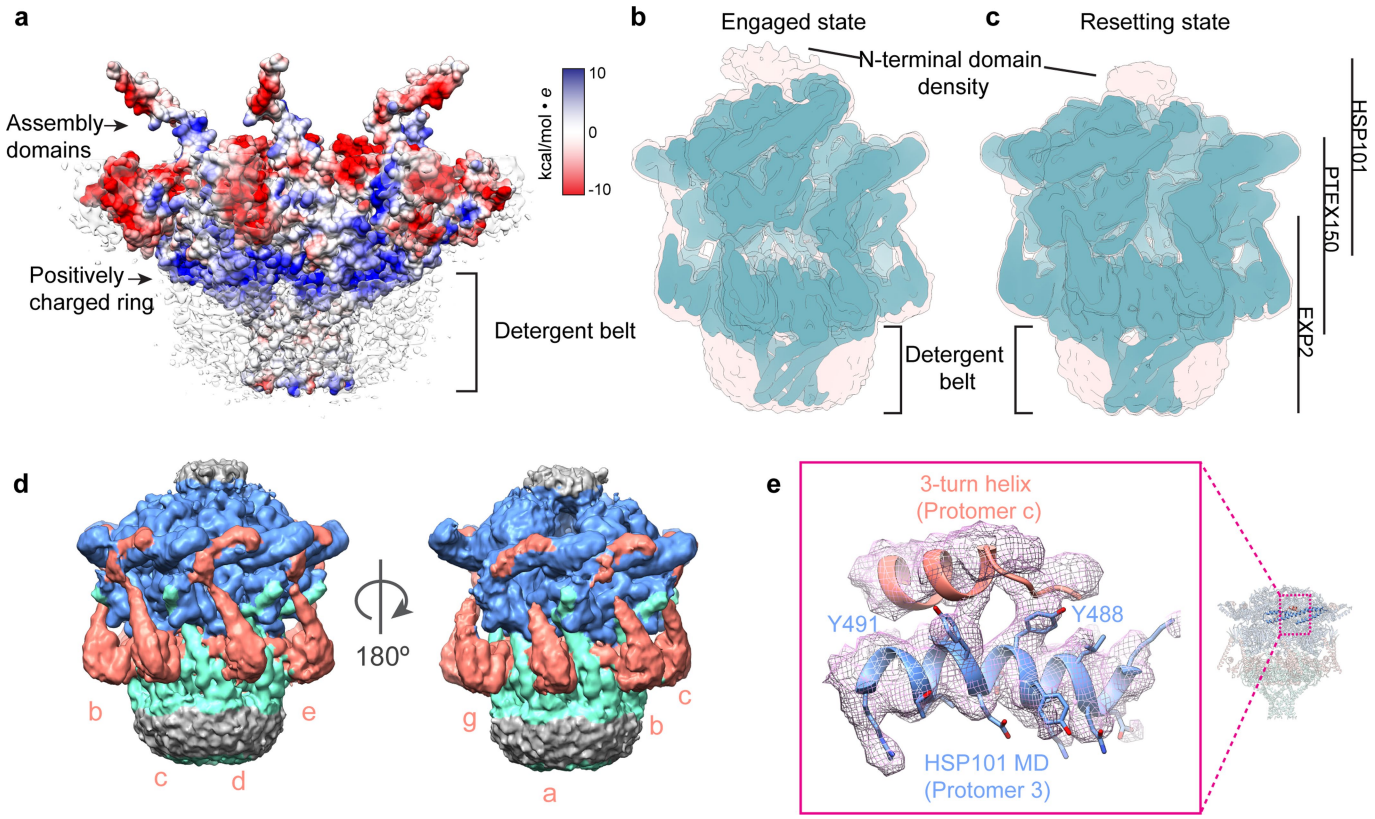

Extended Data Fig. 8 | Detergent belt, amino-terminal domain, and claw densities visible in maps at lower thresholds. a, The engaged state PTEX150–EXP2 heptamer, displayed in surface representation and coloured by electrostatic potential. The bottom half of the full engaged state density map is superimposed, showing the location of the detergent belt in relation to the EXP2 transmembrane domain. A ring of positively charged residues is clearly visible directly above where the PVM surface would normally lie. **b**, **c**, Engaged state (**b**) and resetting state (**c**) maps were low-pass filtered to 6 Å to improve clarity of low-resolution details, and are shown overlaid, at two different thresholds to improve visibility of the detergent belt and the poorly resolved N-terminal domains of HSP101 (teal, higher threshold; peach, lower threshold). **d**, Resetting state map of PTEX displayed at a lower threshold to show the strong claw-shaped densities extending from the PTEX150(668–823) shaft up to the HSP101 M domain. **e**, Enlarged view of the interaction between HSP101 Y488 and Y491 and the three-turn helix, shown with corresponding cryo-EM density (mesh).

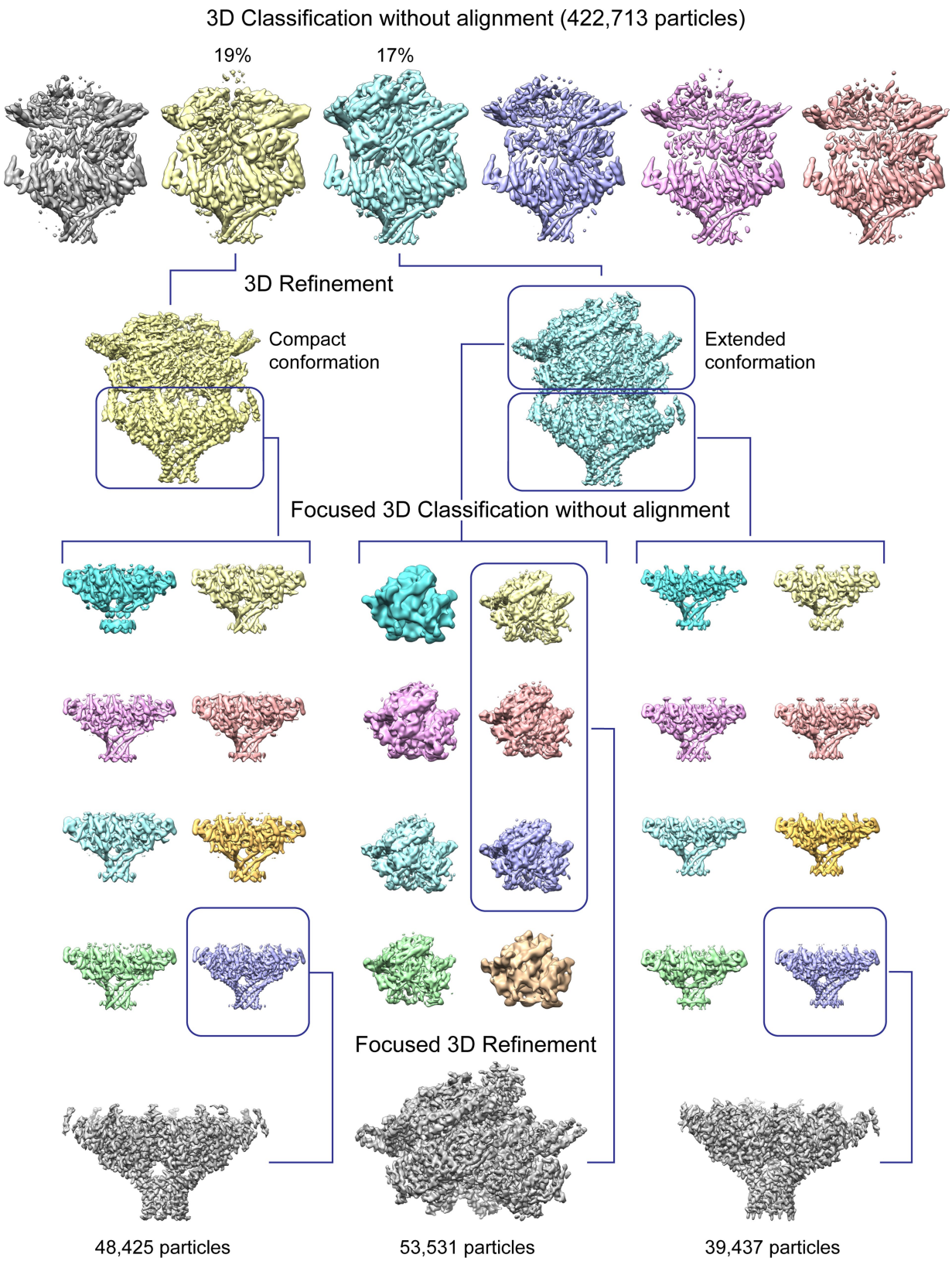

Extended Data Fig. 9 | Data processing workflow. Illustration of workflow for 3D classification, focused classification and refinement. Maps are displayed at higher thresholds where the detergent belt is not visible for clarity, to avoid obscuring details of the transmembrane helices.

Extended Data Table 1 | Cryo-EM data collection, refinement and validation statistics

	PTEX *Engaged* Full (EMDB-8951) (PDB 6E10)	PTEX *Engaged* Top (EMDB-8951) (PDB 6E10)	PTEX *Engaged* Bottom (EMDB-8951) (PDB 6E10)	PTEX *Resetting* Full (EMDB-8952) (PDB 6E11)	PTEX *Resetting* Top (EMDB-8952) (PDB 6E11)	PTEX *Resetting* Bottom (EMDB-8952) (PDB 6E11)
Data collection and processing						
Magnification	×105,000	×105,000	×105,000	×105,000	n/a	×105,000
Voltage (kV)	300	300	300	300	n/a	300
Electron exposure (e–/Å²)	60	60	60	60	n/a	60
Defocus range (μm)	-1.5 to -4.0	-1.5 to -4.0	-1.5 to -4.0	-1.5 to -4.0	n/a	-1.5 to -4.0
Pixel size (Å)	1.04	1.04	1.04	1.04	n/a	1.04
Symmetry imposed	C1	C1	C7	C1	n/a	C7
Initial particle images (no.)	1,508,462	1,508,462	1,508,462	1,508,462	n/a	1,508,462
Final particle images (no.)	72,866	53,531	39,437	78,499	n/a	48,425
Map resolution (Å) FSC threshold	4.09 0.143	4.16 0.143	3.5 0.143	4.23 0.143	n/a	3.4 0.143
Map resolution range (Å)	3.2-7.5	3.0-7.0	2.8-3.6	3.2-7.5	n/a	2.8-3.4
Refinement						
Initial model used (PDB code)	n/a	n/a	n/a	n/a	n/a	n/a
Model resolution (Å) FSC threshold	4.58 0.5	4.23 0.5	3.59 0.5	4.84 0.5	n/a	3.67 0.5
Model resolution range (Å)	4.58	4.23	3.59	4.84	n/a	3.67
Map sharpening *B* factor (Å²)	-180	-180	-170	-180	n/a	-160
Model composition Non-hydrogen atoms Protein residues Ligands	 57,352 6,838 12	 57,352 6,838 12	 57,352 6,838 12	 57,401 6,826 12	 57,401 6,826 12	 57,401 6,826 12
B factors (Å²) Protein Ligand	n/a	n/a	n/a	n/a	n/a	n/a
R.m.s. deviations Bond lengths (Å) Bond angles (°)	 0.008 1.311	 0.009 1.262	 0.008 0.925	 0.008 1.300	 0.007 1.332	 0.006 0.895
Validation MolProbity score Clashscore Poor rotamers (%)	 1.95 9.74 1.04	 1.81 7.35 0.13	 1.53 4.01 0.45	 2.03 10.44 0.47	 1.96 7.46 0.05	 1.64 5.48 0.33
Ramachandran plot Favored (%) Allowed (%) Disallowed (%)	 93.96 5.53 0.51	 94.01 5.76 0.23	 94.99 4.69 0.33	 91.91 7.65 0.44	 89.98 9.58 0.44	 94.98 5.08 0.00

nature research

Corresponding author(s): Z. Hong Zhou

Reporting Summary

Nature Research wishes to improve the reproducibility of the work that we publish. This form provides structure for consistency and transparency in reporting. For further information on Nature Research policies, see Authors & Referees and the Editorial Policy Checklist.

Statistical parameters

When statistical analyses are reported, confirm that the following items are present in the relevant location (e.g. figure legend, table legend, main text, or Methods section).

n/a	Confirmed	
☐	☒	The exact sample size (*n*) for each experimental group/condition, given as a discrete number and unit of measurement
☐	☒	An indication of whether measurements were taken from distinct samples or whether the same sample was measured repeatedly
☐	☒	The statistical test(s) used AND whether they are one- or two-sided *Only common tests should be described solely by name; describe more complex techniques in the Methods section.*
☒	☐	A description of all covariates tested
☒	☐	A description of any assumptions or corrections, such as tests of normality and adjustment for multiple comparisons
☐	☒	A full description of the statistics including central tendency (e.g. means) or other basic estimates (e.g. regression coefficient) AND variation (e.g. standard deviation) or associated estimates of uncertainty (e.g. confidence intervals)
☐	☒	For null hypothesis testing, the test statistic (e.g. *F*, *t*, *r*) with confidence intervals, effect sizes, degrees of freedom and *P* value noted *Give P values as exact values whenever suitable.*
☒	☐	For Bayesian analysis, information on the choice of priors and Markov chain Monte Carlo settings
☒	☐	For hierarchical and complex designs, identification of the appropriate level for tests and full reporting of outcomes
☒	☐	Estimates of effect sizes (e.g. Cohen's *d*, Pearson's *r*), indicating how they were calculated
☐	☒	Clearly defined error bars *State explicitly what error bars represent (e.g. SD, SE, CI)*

Our web collection on statistics for biologists may be useful.

Software and code

Policy information about availability of computer code

Data collection	Leginon, EMMENU4, Zeiss Axiovision, FACS Diva (BD Biosciences), ImageStudio (Li-Cor).
Data analysis	Gautomatch, MotionCor2, CTFFIND4, RELION1.4, RELION2.0, CryoSparc, HOLE, Pymol, UCSF Chimera, Resmap, Molprobity, Coot, PHENIX , Prism (Graphpad), Volocity (Perkin Elmer)

For manuscripts utilizing custom algorithms or software that are central to the research but not yet described in published literature, software must be made available to editors/reviewers upon request. We strongly encourage code deposition in a community repository (e.g. GitHub). See the Nature Research guidelines for submitting code & software for further information.

Data

Policy information about availability of data

All manuscripts must include a data availability statement. This statement should provide the following information, where applicable:

- Accession codes, unique identifiers, or web links for publicly available datasets
- A list of figures that have associated raw data
- A description of any restrictions on data availability

The atomic models and the cryoEM density maps will be deposited to the Protein Data Bank and the Electron Microscopy Data Bank, under the accession numbers of 6E10, 6E11, EMD-8952 and EMD-8951, respectively.

Field-specific reporting

Please select the best fit for your research. If you are not sure, read the appropriate sections before making your selection.

☒ Life sciences ☐ Behavioural & social sciences ☐ Ecological, evolutionary & environmental sciences

For a reference copy of the document with all sections, see nature.com/authors/policies/ReportingSummary-flat.pdf

Life sciences study design

All studies must disclose on these points even when the disclosure is negative.

Sample size	3D reconstructions were calculated from thousands of particle images. This number was determined based on resolutions measured by the Resmap program to be ~2.8-4.5 angstroms, with visible densities for different amino acid residue sidechains.
Data exclusions	about 67% of the total particle images were discarded after 2D and 3D classification using the program RELION.
Replication	Parasite growth and export assay data was collected from cells cultured in two different donor blood samples in experiments performed independently. All attempts at replication were successful.
Randomization	In parasite growth and export assays, samples were + or - aTc treatment to facilitate expression or knockdown of exp2, respectively. In export assays, individual cells analyzed in these conditions were selected by choosing fields using DAPI stain (blind to the experimental channels). All single infected cells in each chosen field were incorporated into the analysis as described in the methods.
Blinding	Immuno fluorescence image acquisition for export assays was performed blind to the experimental channels using the DAPI channel as described in the methods.

Reporting for specific materials, systems and methods

Materials & experimental systems

n/a	Involved in the study
☐	☒ Unique biological materials
☐	☒ Antibodies
☐	☒ Eukaryotic cell lines
☒	☐ Palaeontology
☒	☐ Animals and other organisms
☐	☒ Human research participants

Methods

n/a	Involved in the study
☒	☐ ChIP-seq
☐	☒ Flow cytometry
☒	☐ MRI-based neuroimaging

Unique biological materials

Policy information about availability of materials

Obtaining unique materials	Unique materials are available from authors.

Antibodies

Antibodies used	The following primary antibodies were used for IFA and western blot: mouse anti-FLAG mAb clone M2 (Sigma, catalog # F1804) (IFA: 1:500, WB 1:500); rabbit polyclonal anti-SBP1 [Ref 59] (IFA: 1:500); mouse anti-cMYC mAb 9E10 (ThermoFisher catalog # 13-2500) (WB: 1:300). The following secondary antibodies were used for IFA and western blot: Alexa Fluor Goat anti-Mouse 488 IgG (ThermoFisher catalog # A11029) (IFA: 1:2,000); Alexa Fluor Goat anti-Rabbit 594 IgG (ThermoFisher catalog # A11037) (IFA: 1:2,000); IRDye 680RD Goat anti-Mouse IgG (Li-cor catalog # 925-68070) (WB: 1:10,000); IRDye 800CW Goat anti-Mouse IgG (Li-cor catalog # 925-32210) (WB: 1:10,000). Lot numbers are not available for commercial antibodies.
Validation	For antibodies against epitope tags, untagged parental parasite lines were used to validate specificity in western blot as shown in Figure 4 and Extended Data Figure 1. The antibody against the unique parasite antigen SBP1 has been previously validated: see references 59 and 12.

Eukaryotic cell lines

Policy information about cell lines

Cell line source(s)	The Plasmodium falciparum NF54attB line used in this study was obtained from the Fidock lab where it was generated.
Authentication	PCR amplified regions from the NF54attB genome were found to match the genome sequence for 3D7, a sub clone of NF54. The prescence of the cg6 localized attB sequence was verified by successful Bxb1 integration at that site.
Mycoplasma contamination	Cell lines were not tested for mycoplasma contamination.
Commonly misidentified lines (See ICLAC register)	No commonly misidentified lines were used in the study.

Human research participants

Policy information about studies involving human research participants

Population characteristics	Red blood cells were obtained from deidentified donors under an IRB-exempted protocol. No information about the donors is known.
Recruitment	See above.

Flow Cytometry

Plots

Confirm that:

☒ The axis labels state the marker and fluorochrome used (e.g. CD4-FITC).

☒ The axis scales are clearly visible. Include numbers along axes only for bottom left plot of group (a 'group' is an analysis of identical markers).

☒ All plots are contour plots with outliers or pseudocolor plots.

☒ A numerical value for number of cells or percentage (with statistics) is provided.

Methodology

Sample preparation	Cultured red blood cells infected with Plasmodium falciparum were directly diluted 1:20 into PBS containing acridine orange and immediately analyzed.
Instrument	BD Biosciences FACSCanto
Software	FACSDiva was used for collection and analysis.
Cell population abundance	Cell populations were all Plasmodium falciparum infected red blood cells. These populations varied from ~1% to about 10% of the total red blood cells infected in the cultures evaluated.
Gating strategy	All red blood cells were gated by FSC/SSC. This population was then gated by FITC and PerCP-Cy5.5. The gate was defined by analysis of uninfected red blood cells and drawn to include all events with signal over the uninfected controls (indicating the presence of nucleic acid as a proxy for parasite infection of the anucleate red cells). This simple gating strategy was used to quantify the number of infected red blood cells in parasite growth assays.

☒ Tick this box to confirm that a figure exemplifying the gating strategy is provided in the Supplementary Information.